



HAL
open science

Biased activation of the vasopressin V2 receptor probed by NMR, paramagnetic ligands, and molecular dynamics simulations

Aurelien Fouillen, Pierre Couvineau, Gérald Gaibelet, Stéphanie Riché, Hélène Orcel, Christiane Mendre, Ali Kanso, Romain Lanotte, Julie Nguyen, S Urbach, et al.

► To cite this version:

Aurelien Fouillen, Pierre Couvineau, Gérald Gaibelet, Stéphanie Riché, Hélène Orcel, et al.. Biased activation of the vasopressin V2 receptor probed by NMR, paramagnetic ligands, and molecular dynamics simulations. Computational and Structural Biotechnology Journal, In press, 10.1016/j.csbj.2024.10.039 . hal-03756232v2

HAL Id: hal-03756232

<https://hal.science/hal-03756232v2>

Submitted on 29 Oct 2024

HAL is a multi-disciplinary open access archive for the deposit and dissemination of scientific research documents, whether they are published or not. The documents may come from teaching and research institutions in France or abroad, or from public or private research centers.

L'archive ouverte pluridisciplinaire **HAL**, est destinée au dépôt et à la diffusion de documents scientifiques de niveau recherche, publiés ou non, émanant des établissements d'enseignement et de recherche français ou étrangers, des laboratoires publics ou privés.



Distributed under a Creative Commons Attribution - NonCommercial - NoDerivatives 4.0 International License



Research article

Biased activation of the vasopressin V2 receptor probed by molecular dynamics simulations, NMR and pharmacological studies

Aurélien Fouillen^{a,1}, Pierre Couvineau^{a,1}, Gérald Gaibelet^{a,1}, Stéphanie Riché^b, Hélène Orcel^a, Christiane Mendre^a, Ali Kanso^a, Romain Lanotte^a, Julie Nguyen^a, Juliette Dimon^a, Serge Urbach^a, Rémy Soumier^a, Sébastien Granier^a, Dominique Bonnet^b, Xiaojing Cong^{a,*}, Bernard Mouillac^{a,*}, Hélène Déméné^{c,2,*}

^a Institut de Génétique Fonctionnelle, Université de Montpellier, CNRS, INSERM, 34094 Montpellier, France

^b Laboratoire d'Innovation Thérapeutique, UMR7200 CNRS, Université de Strasbourg, Institut du Médicament de Strasbourg, 67412 Illkirch-Graffenstaden, France

^c Centre de Biologie Structurale (CBS), Univ Montpellier, INSERM, CNRS, 34090, Montpellier, France

ARTICLE INFO

Keywords:

G-protein coupled receptor
Biased Activation
NMR
Molecular dynamics
Enhanced sampling
Pharmacology

ABSTRACT

G protein-coupled receptors (GPCRs) control critical cell signaling. Their response to extracellular stimuli involves conformational changes to convey signals to intracellular effectors, among which the most important are G proteins and β -arrestins (β Arres). Biased activation of one pathway is a field of intense research in GPCR pharmacology. Combining NMR, site-directed mutagenesis, molecular pharmacology, and molecular dynamics (MD) simulations, we studied the conformational diversity of the vasopressin V2 receptor (V2R) bound to different types of ligands: the antagonist Tolvaptan, the endogenous unbiased agonist arginine-vasopressin, and MCF14, a partial Gs protein-biased agonist. A double-labeling NMR scheme was developed to study the receptor conformational changes and ligand binding: V2R was subjected to lysine ¹³CH₃ methylation for complementary NMR studies, whereas the agonists were tagged with a paramagnetic probe. Paramagnetic relaxation enhancements and site-directed mutagenesis validated the ligand binding modes in the MD simulations. We found that the bias for the Gs protein over the β Arr pathway involves interactions between the conserved NPxxY motif in the transmembrane helix 7 (TM7) and TM3, compacting helix 8 (H8) toward TM1 and likely inhibiting β Arr signaling. A similar mechanism was elicited for the pathogenic mutation I130N, which constitutively activates the Gs proteins without concomitant β Arr recruitment. The findings suggest common patterns of biased signaling in class A GPCRs, as well as a rationale for the design of G protein-biased V2R agonists.

1. Introduction

GPCRs, the largest protein family in the human genome, are key players in cell signaling. They share a common architecture composed of an extracellular N-terminal part, a core of seven transmembrane helices (TM1-TM7), followed by a short cytosolic helix (H8) juxtaposed to a disordered C-terminal fragment of variable length. As transmembrane receptors, they sense extracellular stimuli and trigger signal transduction cascades inside the cell, principally via G protein and β Arr pathways [1]. GPCR ligands may preferentially modulate some signaling pathways over others. This functional selectivity is known as GPCR lig-

and bias [2], which enables better control of therapeutic effects, opening new avenues to drug discovery. GPCR-biased signaling may even occur in the *apo* state, in certain constitutively active (often pathological) mutants [3,4].

Both X-ray crystallography and cryo-electron microscopy (cryo-EM) revealed remarkably unified structural rearrangements upon class A GPCR activation stabilized by G proteins or β Arres, characterized by an outward displacement of TM6 and an inward movement of TM7 [5–9]. However, receptor conformational changes before coupling with intracellular partners, essential for biased signaling, are highly dynamic and poorly understood. In this context, MD simulations and spectroscopies

* Corresponding authors.

E-mail addresses: xiaojing.cong@igf.cnrs.fr (X. Cong), bernard.mouillac@igf.cnrs.fr (B. Mouillac), helene.demene@cbs.cnrs.fr (H. Déméné).

¹ These authors contributed equally to this work

² Lead contact: Hélène Déméné, at Centre de Biologie Structurale, Université de Montpellier, INSERM, CNRS, 29, rue de Navacelles, 34090 Montpellier Cedex, France.

<https://doi.org/10.1016/j.csbj.2024.10.039>

Received 15 July 2024; Received in revised form 22 October 2024; Accepted 22 October 2024

2001-0370/© 20XX

in solution, such as NMR or fluorescence, have provided valuable dynamic information to bridge the gap with static structures [10–17], although it is crucial to define how the elicited mechanisms can be extended to other GPCRs [13,18–22].

V2R regulates the renal antidiuretic response in mammals [23]. Binding of arginine-vasopressin (AVP) to V2R activates both Gs protein and β Arr pathways associated with urine concentration [23] and cell growth/proliferation, respectively [24,25]. V2R is a major therapeutic target for water balance disorders [26]. Loss-of-function mutations result in the congenital nephrogenic diabetes insipidus (cNDI) [27], characterized by excessive urine voiding and dehydration [28]. The mutant receptors are usually misfolded and retained in the endoplasmic reticulum [29]. A class of benzazepine compounds, the MCF series, has been found to rescue expression and signaling of some cNDI mutants. These compounds display promising biased profiles of long-lasting activation of the Gs protein pathway, without triggering β Arr-mediated internalization [30]. Conversely, some pathological gain-of-function V2R mutations lead to the nephrogenic syndrome of inappropriate antidiuresis (NSIAD), characterized by hyponatremia [31]. Several of these mutants, such as I130^{3,43}N (superscript refers to Ballesteros-Weinstein nomenclature, where the first number denotes the helix and the second the residue position relative to the most conserved position) [32], display constitutive activities only for Gs proteins, mimicking GPCR-biased signaling [33–35].

High-resolution structures of V2R active states in complex with AVP and either Gs [36–38] or β Arr1 proteins [39] have been recently obtained by us and others. No structure of V2R in an inactive or biased state is yet available. Hence, little is known about V2R ligand or mutation-induced bias and dynamics, apart from our preliminary fluorescence study suggesting that AVP and the Gs-biased agonist MCF14 induced distinct V2R conformations on the intracellular side of TM7 and H8 [12]. Here, we combined MD simulations, functional cell pharmacology, site-directed mutagenesis and NMR spectroscopy, to identify these conformations, in comparison with those induced by the antagonist Tolvaptan (TVP). An enhanced-sampling MD technique was used to capture millisecond-timescale events with microseconds of simulations. The technique has proven effective in monitoring GPCR activation [40, 41] allowing direct comparison with NMR data [13,40–42]. To assess the predicted ligand binding poses, we used site-directed mutagenesis and a double-labeling scheme using lysine ¹³CH₃ methylation on V2R and paramagnetic tagging of the ligands (Fig. S1). The recorded Paramagnetic Relaxation Enhancement (PRE) data were in agreement with the measurements from MD simulations. We identified distinct receptor conformations associated with the Gs-biased agonist, which were also observed in the constitutively Gs-active mutant I130^{3,43}N. The results pinpointed the role of specific TM3-TM7 interactions involving the pivotal NP^{7,50}xxY motif in Gs-biased V2R activation.

2. Material and methods

2.1. Molecular dynamic simulations

2.1.1. Setup of MD simulations

The initial models of V2R in inactive state were built using Modeller v9.15 [43] based on the cryo-EM structures of AVP-V2R-Gs complexes (PDBs 7DW9 [37], and 7BB6 [36]) and the X-ray crystal structure of the oxytocin receptor in an inactive state (PDB 6TPK [44]). In this model, the intracellular half of V2R was based on the oxytocin receptor inactive state. The *apo* wild-type (WT) and mutant forms were generated using the same procedure, excluding AVP. The MCF14 and TVP bound forms were obtained by docking the ligands to the *apo* forms, using Autodock Vina [45]. A grid box was set to encompass the pocket with a 0.375 Å grid point spacing. Ligands and pocket residues were set flexible during docking. Paramagnetic tags were added to the ligand-bound forms above. The linker to the paramagnetic tag in ^{para}MCF14 was gen-

erated in an arbitrary initial conformation [45]. PACKMOL-Memgen [46] was used to assign the side-chain protonation states and embed the models in a lipid bilayer of POPC and cholesterol in 3:1 ratio. The systems were solvated in a periodic 78 × 78 × 112 Å³ box of explicit water and neutralized with 0.15 M of Na⁺ and Cl⁻ ions. We used the Amber ff14SB [47], GAFF2 [48] and lipid14 [49] force fields, the TIP3P water models [50] and the Joung-Cheatham ion parameters [51]. Effective point charges of the ligands were obtained by RESP fitting [52] of the electrostatic potentials calculated with Gaussian16 and the HF/6–31 G* basis set. After energy minimization, all-atom MD simulations were carried out using Gromacs 2020 [53] patched with the PLUMED 2.3 plugin [54]. Each system was gradually heated to 310 K and pre-equilibrated during 10 ns of brute-force MD in the *NPT*-ensemble. The replica exchange with solute scaling (REST2)[55] technique was used to enhance the MD sampling. Microseconds of REST2 MD can capture GPCR conformational dynamics at the millisecond timescale. We performed 100 ns × 64 replicas (6.4 μs) of REST2 MD in the *NVT* ensemble for each system. The first 20 ns were discarded for equilibration. The trajectories of the original unmodified replica were collected and analyzed.

2.1.2. Principle of REST2

REST2 [55] is a type of Hamiltonian replica exchange simulation scheme, which performs many replicas of the same MD simulation system in parallel with the original system (Fig. S2). The replicas have modified free energy surfaces to facilitate barrier crossing. By frequently swapping the replicas and the original system during the MD, the simulations “travel” on different free energy surfaces and easily visit different conformational zones. Finally, only the samples in the original system (with unmodified free energy surface) are collected. The replicas are artificial and are only used to overcome the energy barriers. REST2 modifies the free energy surfaces by scaling (reducing) the force constants of the “solute” molecules in the simulation system. In this case, the protein and the ligands were considered as “solute”—the force constants of their van der Waals, electrostatic and dihedral terms were subject to scaling—in order to facilitate their conformational changes. The effective temperatures used here for generating the REST2 scaling factors ranged from 310 K to 1000 K for 64 replicas, following a distribution calculated with the Patriksson-van der Spoel approach [56]. Exchange between the replicas was attempted every 1000 simulation steps. This setup resulted in an average exchange probability of ~30 % throughout the simulation course.

2.2. V2R construction and expression

The V2R construct used for the NMR analysis was described previously [36]. It is also shown in Fig. S1A. Briefly, the *Spodoptera frugiperda* (*Sf9*)-optimized sequence of the human V2R was cloned into a pFastBacTM1 vector (ThermoFisher Scientific) using EcoR1/Xba1 restriction sites. To facilitate expression and purification of the V2R construct, the hemagglutinin signal peptide (MKTHIALSYIFCLVFA) followed by a Flag-tag (DYKDDDDA) were added at the N-terminus, and a Twin-strep-tag® (WSHPQFEKGGGSGGGSGGGWSHPQFEK) inserted at the C-terminus. In addition, N22 was substituted with a glutamine residue to avoid N-glycosylation, and C358 mutated into an alanine to eliminate potential intermolecular disulfide bridges during solubilization and purification. A Tobacco Etch Virus (TEV) protease cleavage site (ENLYFQG - following the Flag-tag) and 2 Human Rhinovirus 3 C protease (HRV3C) cleavage sites (LEVLVQGP - one inserted in the N-terminus between D30 and T31, the other inserted in the C-terminus between G345 and Q354 and replacing R346-TPPSLG-P353) were also added to remove N and C termini and facilitate NMR analysis (Fig. S1A). After cleavage, the resulting sequence corresponds to a 323 amino-acid residue protein with a theoretical 35.5 kDa molecular weight. M1L2 residues were replaced by AS residues, and LE residues

were added before the Twin-strep-tag®, during subcloning (introduction of Nhe1 and Xho1 restriction sites, respectively). Sequence modifications did not affect the receptor ligand binding or function [36]. The V2R was expressed in Sf9 insect cells using the Bac-to-Bac® baculovirus expression system (Invitrogen) according to manufacturer's instructions. Insect cells were grown in suspension in EX-CELL® 420 medium (Sigma-Aldrich) to a density of 4×10^6 cells per ml and infected with the recombinant baculovirus encoding V2R at a multiplicity of infection of 2 to 3. The culture medium was supplemented with the specific V2R pharmacochaperone antagonist Tolvaptan (Sigma-Aldrich) at 1 μ M to allow proper folding and membrane targeting of the receptor [30,57]. The cells were infected for 48 h to 54 h at 28 °C. Before harvesting, the expression of the V2R was controlled by immunofluorescence using an anti-Flag M1 antibody coupled to an Alexa-488 fluorophore (ThermoFisher Scientific). Cells were then harvested by centrifugation (2 steps, 15 min then 20 min at 3000 g) and the cell pellets were stored at -80 °C until use.

The different NMR mutants of the V2R (V2R^{K100R}, V2R^{K116R}, V2R^{K268R}, V2R^{R64K-K100R}) were all derived from the matrix described above using the gene synthesis and molecular biology services of Eurofins Genomics.

2.3. V2R purification and labeling

After thawing the frozen cell pellets, resulting typically from 24 culture liters, cells were lysed by osmotic shock in 10 mM Tris-HCl pH 8, 1 mM EDTA buffer containing 2 mg.ml⁻¹ iodoacetamide (Sigma-Aldrich), Tolvaptan 1 μ M and protease inhibitors [leupeptine (5 μ g.ml⁻¹) (Euromedex), benzamidine (10 μ g.ml⁻¹) (Sigma-Aldrich), and phenylmethylsulfonyl fluoride (PMSF) (10 μ g.ml⁻¹) (Sigma-Aldrich)]. Lysed cells were centrifuged (15 min at 38,400 g) and the pellets containing crude membranes were solubilized using a glass dounce tissue grinder (15 + 20 strokes using A and B pestles respectively) in a solubilization buffer containing 20 mM Tris-HCl pH 8, 500 mM NaCl, 0.5 % (w/v) n-dodecyl- β -D-maltopyranoside (DDM, Anatrace), 0.2 % (w/v) sodium cholate (Sigma-Aldrich), 0.03 % (w/v) cholesteryl hemisuccinate (CHS, Sigma-Aldrich), 20 % Glycerol (VWR), 2 mg.ml⁻¹ iodoacetamide, 0.75 mL.L⁻¹ Biotin Bioblock (IBA), Tolvaptan 1 μ M and protease inhibitors. The extraction mixture was stirred for 1 h at 4 °C and centrifuged (20 min at 38,400 g).

The cleared supernatant was poured onto equilibrated Strep-Tactin resin (IBA) for a first affinity purification step. After 2 h of incubation at 4 °C under stirring, the resin was laid down into a column and washed three times with 10 column volume (CV) of a buffer containing 20 mM Tris-HCl pH 8, 500 mM NaCl, 0.1 % (w/v) DDM, 0.02 % (w/v) sodium cholate, 0.03 % (w/v) CHS, Tolvaptan 1 μ M. The bound receptor was eluted in the same buffer supplemented with 2.5 mM Desthiobiotin (IBA). The amount of V2R was calculated by UV absorbance spectroscopy.

The eluate supplemented with 2 mM CaCl₂ was loaded onto an M1 anti-Flag affinity resin (Sigma-Aldrich) for a second affinity purification. After loading, the DDM detergent was then gradually exchanged into a buffer with Lauryl Maltose Neopentyl glycol (LMNG, Anatrace) (20 mM HEPES pH 7.4, 100 mM NaCl, 0.01 % CHS and 0.5 % LMNG). The LMNG concentration was then decreased from 0.5 % to 0.02 %. The V2R was then eluted in 20 mM HEPES pH 7.4, 100 mM NaCl, 0.02 % LMNG, 0.002 % CHS, 2 mM EDTA, 10 μ M Tolvaptan and 0.2 mg.ml⁻¹ Flag peptide (Covalab). The absence of Tolvaptan during the SEC, the two dialysis steps and during the final dilution /concentration of the sample ensured that the orthosteric binding site of the V2R was empty and available for measuring effects of the different biased and unbiased ligands. The amount of V2R was estimated by UV absorbance spectroscopy and was then cleaved overnight using the HRV3C protease at a 1:20 wt ratio (HRV3C:V2R) at 4 °C. Concomitantly, the V2R was labeled onto its lysine residues by reductive methylation

using 10 mM ¹³C-formaldehyde (Sigma-Aldrich) in the presence of 10 mM sodium cyanoborohydride (Sigma-Aldrich) following the protocol described previously [58,59].

The HRV3C-cleaved ¹³C-dimethyl-lysine-labeled V2R was concentrated using 50-kDa concentrators (Merck Millipore) and separated from the protease using a Superdex 200 10/300 column on an AKTA purifier system (0.5 ml/min flowrate, buffer 20 mM HEPES pH 7.4, 100 mM NaCl, 0.02 % MNG, no ligand). Fractions corresponding to the pure monomeric V2R were pooled and dialyzed first 2 h at 4 °C using a 3-kDa MWCO cassette (ThermoFisher Scientific) in 20 mM HEPES pH 7.4, 40 mM NaCl, 0.02 % LMNG, 0.002 % CHS. Then, the sample was dialyzed again 2 h at 4 °C in 98.85 % D₂O buffer with 20 mM HEPES-d18 pH 7.4 (uncorrected), 40 mM NaCl, 0.02 % LMNG, 0.002 % CHS. V2R was then concentrated using a 50-kDa MWCO concentrator up to 250 μ l, and then diluted with 2 ml of 98.85 % D₂O buffer with 20 mM HEPES-d18 pH 7.4, 40 mM NaCl before a second concentration step. The final concentration of V2R was 25–30 μ M in buffer containing 20 mM HEPES-d18 pH 7.4, 40 mM NaCl, 0.0022 % LMNG and 0.0002 % CHS (NMR buffer). Acid 4,4-dimethyl-4-silapentane-1-sulfonate (DSS) was added at a final concentration of 100 μ M as a standard to calibrate the NMR analysis.

2.4. Mass spectrometry and NMR analysis of lysine methylation

Samples were prepared as previously described [39]. We used V2R^{K100R} to better assign the NMR signals from K268^{6,32}. Briefly, to perform these experiments, the V2R^{K100R} mutant was expressed, extracted and purified. Following the M1 anti-flag affinity chromatography, the receptor was cleaved by the HRV3C protease and concomitantly labelled (or not) onto its lysine residues by reductive methylation. At this step, only two residues can be labelled, K116 and K268 (see Fig S1A). Then, the samples were concentrated, subjected to size exclusion chromatography, and the eluted fractions concentrated to 1 μ g/ μ l. The purified V2R^{K100R}, labelled or unlabelled (10 μ g per sample), was digested using S-Trap micro columns (<https://protifi.com/>; Huntington, NY) following the supplier's protocol using 1 μ g of trypsin (Promega, Gold) for 2 h at 47 °C. The peptides obtained were analyzed using nano-throughput high-performance liquid chromatography (Ultimate 3000-RSLC, Thermo Fisher Scientific) coupled to a mass spectrometer (Q Exactive-HF, Thermo Fisher Scientific) equipped with a nanospray source. Raw spectra were processed using the MaxQuant v2.0.3.0 [60]. Signal intensities of receptor peptides were extracted using Skyline v21.1.0.245 [47]. Graphical representation of the spectra was performed using FreeStyle v1.8 SP2 (Thermo Fisher Scientific Inc.). NMR analysis of lysine methylation was done by inspecting the 2.4–3 ppm/¹H/¹³C regions (monomethyls) and 2.4–3 ppm/¹H/¹³C regions (dimethyls) of HMQC spectra.

2.5. Synthesis of paramagnetic ligands

2.5.1. General

Reagents were obtained from commercial sources and used without any further purification. (Deamino-Cys¹, Lys⁸)-Vasopressin trifluoroacetate was purchased from Bachem. Compound 1 was synthesized as previously described [61]. Thin-layer chromatography was performed on Merck silica gel 60F254 plates. VWR silica gel (40–63 μ m) was used for chromatography columns. Semi-preparative reverse-phase HPLC purifications were performed on a Waters SunFire C18 OBD Prep column (5 μ m, 19 \times 150 mm) on a Gilson PLC2020 system. Analytical reverse-phase HPLC were performed on a Ascentis C18 column (2.7 μ m, 7.5 cm \times 4.6 mm) on an Agilent Technologies 1200 series HPLC system using a linear gradient (5 % to 100 % v/v in 7.3 min, flow rate of 1.6 ml.min⁻¹) of solvent B (0.1 % v/v TFA in CH₃CN) in solvent A (0.1 % v/v TFA in H₂O). ¹H NMR spectra were recorded at 400 MHz, ¹³C NMR spectra were recorded at 101 MHz on a Bruker Avance spec-

trometer. Chemical shifts are reported in parts per million (ppm), and coupling constants (J) are reported in hertz (Hz). Signals are described as s (singlet), d (doublet), t (triplet), q (quadruplet), p (pentuplet) and m (multiplet). High-resolution mass spectra (HRMS) were obtained on an Agilent Technologie 6520 Accurare-Mass Q.Tof LC/MS apparatus equipped with a Zorbax SB C18 column (1.8 μ m, 2.1 \times 50 mm) using electrospray ionization (ESI) and a time-of-flight analyzer (TOF).

2.5.2. ^{par}MCF14

The synthesis of ^{par}MCF14 was performed in two steps (Fig. S3A).

Tert-butyl (6-((1-(2-chloro-4-(3-methyl-1H-pyrazol-1-yl) benzoyl)-2,3,4,5-tetrahydro-1H-benzo[b]azepin-5-yl)oxy)hexyl) carbamate (compound 2). To a solution of compound 1 (281.6 mg, 0.74 mmol) in 20 ml of anhydrous DMF at 0 °C under argon atmosphere was added NaH 60 % (70.7 mg, 1.84 mmol) portion wise. After 15 min, tert-butyl N-(6-bromohexyl) carbamate (517 mg, 1.84 mmol) in 8 ml of anhydrous DMF was added dropwise and stirred for 18 h at room temperature (RT). The crude product was diluted in saturated aqueous NaHCO₃ and extracted with CH₂Cl₂. The organic phases were dried over Na₂SO₄, and evaporated. The residue was purified by chromatography on a silica gel column (0 % to 30 % EtOAc in *n*-heptane) to afford a clear oil (307 mg; yield 72 %). $t_R = 6.71$ min ¹H RMN (400 MHz, DMSO-*d*₆): δ 8.39–8.37 (m, 1H), 8.04–7.71 (m, 2H), 7.41–7.25 (m, 3H), 7.11–6.96 (m, 2H), 6.83–6.71 (m, 1H), 6.32–6.31 (m, 1H), 4.79–4.74 (m, 1H), 4.53–4.52 (m, 1H), 3.57–3.38 (m, 2H), 2.94–2.73 (m, 3H), 2.37–2.14 (m, 4H), 2.02–1.98 (m, 1H), 1.69–1.52 (m, 4H), 1.41–1.20 (m, 17H). ¹³C (100 MHz, DMSO-*d*₆): δ 165.3, 164.8, 155.5, 150.5, 141.6, 140.1, 139.8, 138.7, 137.4, 133.3, 133.1, 131.5, 130.8, 129.3, 128.8, 128.7, 128.5, 127.7, 127.3, 127.2, 127.1, 117.8, 117.6, 116.5, 115.5, 114.8, 108.5, 81.0, 79.1, 77.7, 77.2, 68.9, 68.2, 46.9, 46.1, 39.8, 32.7, 29.4, 28.2, 26.2, 25.5, 24.9, 22.5, 13.3.

^{par}MCF14. Compound 2 (14 mg, 0.03 mmol) was dissolved in a solution HCl 4 N/Dioxane (400 μ l) and was stirred 30 min at RT and then evaporated. The residue was dissolved in DMF (1 ml) under argon. Then 3-carboxy-PROXYL (6.7 mg, 0.036 mmol) and PyBOP (18.7 mg, 0.04 mmol) were added to the solution followed by DIEA (0.03 ml, 0.18 mmol). Then the resulting mixture was stirred for 1 h and evaporated. The expected compound was isolated by semi-preparative RP-HPLC on a Sunfire RP-C18 column using a linear gradient of solvent B in solvent A. Fractions containing the product were freeze-dried to afford a clear oil (10.7 mg; yield 55 %). $t_R = 5.80$ min. HRMS (EI) *m/z* calcd for C₃₆H₄₈ClN₅O₄ [M + H]⁺ 649.3317, found: 649.3305.

2.5.3. ^{par}dLVP

The synthesis of ^{par}dLVP was performed in one step (Fig. S3B).

To a solution of (deamino-Cys¹, Lys⁸)-Vasopressin trifluoroacetate (2.5 mg, 2.16 μ mol) and 3-carboxy-PROXYL (0.48 mg, 2.6 μ mol) in anhydrous DMF (100 μ l) under argon atmosphere were added DIEA (2.15 μ l, 12.9 μ mol) and PyBOP (1.35 mg, 2.56 μ mol), stirred for 1 h at RT and then evaporated. The expected compound was isolated by semi-preparative RP-HPLC on a Sunfire RP-C18 column using a linear gradient of solvent B in solvent A. Fractions containing the product were lyophilized to afford a white solid (1.7 mg; yield 65 %). $t_R = 3.15$ min. HRMS (EI) *m/z* calcd for C₅₅H₇₉N₁₃O₁₄S₂ [M + H]⁺, 1209.5310, found: 1209.5315.

2.6. NMR spectroscopy

Final samples of V2R (~270 μ l at 30–35 μ M) were loaded into Shigemi microtubes whose susceptibility matched with D₂O. All data for ligands and mutant studies were acquired on 700 MHz Bruker Avance III spectrometers (Bruker, Rheinstetten, Germany), equipped with 5 mm cryogenic H/C/N/D probes with z axis gradient at 293 K, unless otherwise specified. Typically, when possible, the effects of ligands were studied using samples from the same purification batch, cor-

responding to a total volume of cell culture of 20–24 liters. 1H-13C correlation spectra were recorded using heteronuclear multiple-quantum coherence (HMQC) experiments in echo anti-echo mode. Spectral widths in ω_1 and ω_2 were 8417.5 Hz and 3518.6 Hz at 700 MHz centred at 40 p.p.m. ¹³C decoupling was performed with a GARP4 sequence. Thirty-two steady-state scans preceded data acquisition. Typically, 134 complex points with per FID were recorded, to ensure a 27-Hz resolution per point at 700 MHz before zero filling, with 32 scans and a relaxation delay of 1.5 s (^{par}dLVP, ^{par}MCF14) or 80 scans and a relaxation delay of 0.5 s (AVP, MCF14, TVP). Total collection time varied between 3 and 4 h, depending on the sample concentration. Ligands were dissolved in NMR buffer (AVP, ^{par}dLVP) or in perdeuterated dimethyl d₆-sulfoxide (d₆-DMSO, Cambridge Isotope) (MCF14, ^{par}MCF14, TVP) to 10 mM and directly added to the sample before transfer into the Shigemi tube at a final concentration 5- (AVP, MCF14, TVP) or 0.95-fold (^{par}dLVP, ^{par}MCF14) of receptor. The non-paramagnetic agonists (AVP, MCF14, TVP) have high affinities for V2R (< 0.1 μ M). At saturating concentrations (30 μ M and 150 μ M for V2R and non-paramagnetic ligands, respectively), according to the law of mass action, 99 % of the V2R should be in complex at 150 μ M concentration of agonists. The effect of paramagnetic ligands was studied using sub-stoichiometric ligand concentrations, to minimize potential non-specific binding effects. Reduction was achieved by the addition of 5 equivalents of freshly prepared ascorbic acid dissolved at 10 mM in the NMR buffer to the ^{par}MCF14 and ^{par}dLVP-bound preparations, after verification that addition of up to 20 equivalents of ascorbic acid had no effect on the *apo*-V2R spectrum (we used the V2R-K268^{6,32} as a control).

All NMR spectra were processed using the suite of programs provided in the NMRPipe/NMRDraw software distribution [62]. The spectra were normalized using DSS (2,2-dimethyl-2-silapentane-5-sulfonic acid) as an internal reference. For peak fitting analysis with the NMRPipe software, spectra were processed with a Gaussian window, and zero-filled to 4096 \times 1024 data points in time domain data t2 and t1, respectively. Briefly, the g1 parameter corresponding to line sharpening was adjusted so that the time-domain signal no longer decays. The g2 parameter corresponding to line broadening was then selected, with the goal of getting an exponentially well-decayed FID after both g1 and g2 are applied together. Peaks of processed spectra were then fitted with the program nlinLS, provided as a part of the NMRPipe package starting from values obtained from the peak-peaking routine. The nlinLS explicitly takes into account the overlap of peaks, which are fitted simultaneously and not independently by adjusting the parameter Clustid. The quality of the fits was examined visually by estimating the residual difference between the experimental data and the results of the model calculations. Peak intensity of the ¹³C-dimethylated lysines were normalized to the intensity of the G52 (cleaved N terminus) and buffer peaks. Errors in the peak volume were calculated replicating experiments starting purification of different V2R culture batches (AVP, n = 3; ^{par}AVP, n = 2; MCF14, n = 4; ^{par}MCF14, n = 2; TVP, n = 3). Figures were drawn with the Topspin 3.6 (Bruker, Inc) and NMRview packages [63].

2.7. Site-directed mutagenesis of V2R for pharmacological ligand binding assays

To perform the different V2R variants dedicated to binding studies, we mutated multiple V2R residues into an alanine (Q92A, M120A, Q174A, F178A, F287A, and Q291A) using a pRK5 plasmid coding for the human V2R sequence fused at its N-terminus to the enzyme-based self-labeling SNAP-tag (pRK5-SNAP vector, PerkinElmer Revvity). The forward and reverse primers partially overlapped each other to insert each mutation. The enzyme and reaction buffers were commercially available using the KOD Hot Start DNA Polymerase kit (MERK-Millipore). PCR reactions were carried out in a final volume of 50 μ l us-

ing the buffer conditions and enzyme amounts of the manufacturer protocol. In all conditions, reactions included 0.2 mM dNTP, 0.3 μ M of each primer, 1.5 mM $MgSO_4$, and 0.02 U/ μ l of KOD Hot start DNA polymerase and 200 ng of template DNA. The cycling conditions were 2 min at 95 °C, 30 s at oligo's T_m , then 29 cycles at 72 °C for 3 min, and a final cycle at 72 °C for 1 min. Following the PCR reaction, 1 μ l of DPN1 (Biolabs, #R0176S) was then added to the PCR product for 1 h at 37 °C. Then 2.5 μ l of the PCR solution were used to transform 50 μ l of commercially DH5 α competent cells (Life technologies), before to be plated on agar ampicillin plate. Following an overnight growth, bacterial plates were stored at 4 °C. Unique clones for each condition were then picked and grown overnight at 37 °C in 3 ml of LB medium. Finally, we performed plasmid DNA mini-preparations kit (QIAGEN) to transfect HEK cells for binding assays. In addition, all mutated plasmids were sequenced to confirm each mutation with a SP6 primer (ATTTAGGTGACACTATAG) using the molecular biology services of Eurofins Genomics.

2.8. Time-resolved fluorescence resonance energy transfer binding assays

V2R binding studies using Tag-Lite assays (PerkinElmer Revvity) based on time-resolved fluorescence resonance energy transfer (TR-FRET) measurements were previously described [36,64,65]. The technology combines the advantages of FRET with time-resolved measurement of fluorescence, eliminating short-lived background fluorescence. In binding studies, the V2R is labeled with the fluorescence donor (PerkinElmer Revvity), a europium cryptate (Eu cryptate), and the ligand (PerkinElmer Revvity) is labeled with a fluorescence red acceptor, the d2 (DY647). The donor emits fluorescence upon excitation and the energy is transferred to the acceptor if binding occurs, leading to a specific fluorescence signal. The donor fluorescence is also measured and a ratio with the fluorescence applied (665 nm/620 nm, see below). Briefly, HEK cells were plated (15,000 per well) in pre-coated with poly-L-ornithine (14 μ g/ml, Sigma-Aldrich) white-walled, flat-bottom, 96-well plates (Greiner CELLSTAR plate, Sigma-Aldrich) in Dulbecco's minimum essential medium (DMEM) containing 10 % fetal bovine serum (FBS, Eurobio), 1 % nonessential amino acids (GIBCO), and penicillin/streptomycin (GIBCO). Cells were transfected 24 h later with a plasmid coding for the 3C-cleaved V2R version used in NMR studies (Fig S1A) fused at its N-terminus to the enzyme-based self-labeling SNAP-tag (pRK5-SNAP vector, PerkinElmer Revvity). All the mutations were introduced in this V2R construction (Fig. S1A). Transfections were performed with X-tremeGENE 360 (Merck), according to the manufacturer's recommendations: 10 μ l of a premix containing DMEM, X-tremeGENE 360 (0.3 μ l per well), SNAP-V2 coding plasmid (from 10 ng to 100 ng per well, depending on each construct), and noncoding plasmid (up to a total of 100 ng DNA) were added to the culture medium. After a 48-hour culture period, cells were rinsed once with Tag-lite medium (PerkinElmer Revvity) and incubated in the presence of Tag-lite medium containing 100 nM benzylguanine-Lumi4-Tb for at least 60 min at 37 °C. Cells were then washed four times. For saturation studies, cells were incubated for at least 4 h at 4 °C in the presence of benzazepine-red nonpeptide vasopressin antagonist (BZ-DY647, PerkinElmer Revvity) at various concentrations ranging from 10^{-10} to 10^{-7} M. Nonspecific binding was determined in the presence of 10 μ M vasopressin. For competition studies, cells were incubated for at least 4 h at 4 °C with benzazepine-red ligand (5 nM) and increasing concentrations of vasopressin ranging from 10^{-12} to 10^{-5} M. Fluorescent signals were measured at 620 nm (fluorescence of the donor) and at 665 nm (FRET signal) on a PHERAstar (BMG LABTECH). Results were expressed as the 665/620 ratio [$10,000 \times (665/620)$]. A specific variation of the FRET ratio was plotted as a function of benzazepine-red concentration (saturation experiments) or competitor concentration (competition experiment). All binding data were analyzed with GraphPad 9.1.1 (GraphPad Prism Software Inc.) using the one site-specific bind-

ing equation. All results are expressed as the means \pm SEM of at least three independent experiments performed in triplicate. K_i values were calculated from median inhibitory concentration values with the Cheng-Prusoff equation.

2.9. cAMP accumulation assays

V2R (WT and mutants V2R^{K100R}, V2R^{I130N}) functional studies based on TR-FRET measurements were described previously [30,36,66]. Briefly, HEK cells were plated in pre-coated black-walled 96-well plates (Falcon) at 5,000 cells per well, and then transfected 24 h later with a plasmid coding for the SNAP-tagged V2R version used in NMR studies. Transfections were performed with X-tremeGENE 360 (Merck), according to the manufacturer's recommendations: 10 μ l of a premix containing DMEM, X-tremeGENE 360 (0.3 μ l per well), pRK5-SNAP-V2R coding plasmid (ranging from 0.3 to 30 ng per well, depending on the V2R construct), and pRK5 noncoding plasmid (ranging from 70 to 99.7 ng per well) were added to the culture medium. After a 24-hour culture period, cells were treated for 30 min at 37 °C in the cAMP buffer with or without increasing ligands concentrations (10^{-12} to 3.16×10^{-5} M) in the presence of 0.1 mM RO201724, a phosphodiesterase inhibitor (Sigma-Aldrich). The accumulated cAMP was quantified using the cAMP Gs Dynamic Kit (PerkinElmer Revvity) according to the manufacturer's protocol. Native cAMP produced by cells upon activation competes with d2-labeled cAMP (red acceptor) for binding to monoclonal Eu cryptate-labeled antibody (fluorescent donor). The specific signal is inversely proportional to the concentration of cAMP (in the dose-response experiments, the FRET signal is thus decreasing as a function of cAMP increase in the sample). Fluorescent signals were measured at 620 and 665 nm on a PHERAstar microplate reader. Data were plotted as the FRET ratio [$10,000 \times (665/620)$] as a function of AVP concentration [\log (AVP)]. Data were analyzed with GraphPad Prism v 9.1.1 (GraphPad Prism Software Inc.) using the "dose-response stimulation" subroutine. Median effective concentrations were determined using the log(agonist) versus response variable slope (four parameters) fit procedure. Experiments were repeated at least three times on different cultures, each condition in triplicate. Data are presented as means \pm SEM.

2.10. β Arr2 recruitment FRET assays

The recruitment assay of β Arr2 was previously described [39]. Briefly, upon GPCR activation, β Arrestins are recruited to stop G protein signaling and to initiate clathrin-mediated receptor internalization. During this process, the release of the C-terminal domain of β Arrestins is associated with the binding of β Arrestins to the adaptor protein 2 (AP2). This interaction can be measured using the HTRF® technology (PerkinElmer Revvity) based on the use of two specific antibodies, one directed against β Arr2, the second one specific for AP2. In this assay (β Arr2 recruitment kit, PerkinElmer Revvity), the AP2 antibody is labeled with an Eu cryptate fluorescent donor, and the one against β Arr2 is labeled with a d2 fluorescent acceptor, their proximity being detected by FRET signals. The specific signal is positively modulated in proportion with the recruitment of β Arr2 to AP2 upon V2R activation by AVP. Briefly, HEK cells were plated at a seeding density of 25,000 cells per well in a pre-coated white-walled 96-well plates (CELLSTAR plate, Sigma-Aldrich) for 24 h, in DMEM complemented with 10 % FBS, 1 % non-essential amino acids, and 1 % penicillin-streptomycin antibiotics solution. To produce the V2R, the cells were transfected with a pRK5-SNAP-V2R plasmid (from 0.6 to 30 ng per well, depending on the construct, WT or I^{130N} NMR versions) using X-tremeGENE 360 (Merck), according to the manufacturer's recommendations. After a 24-hour culture, cells were used to evaluate the recruitment of β Arr2 to AP2 upon V2R activation with the β Arr2 recruitment kit (PerkinElmer Revvity) following the manufacturer recommendation. Briefly, the cells were first washed one time with DMEM-free and incubated 2 h at RT with 100 μ l per well of

stimulation buffer containing various concentrations of the different ligands (ranging from 10^{-12} M to 10^{-5} M). The medium was then replaced by 30 μ l per well of stabilization buffer for 15 min at RT. The cells were then washed three times with 100 μ l per well of wash buffer before adding 100 μ l per well of a pre-mix of Eu cryptate and d2 antibodies in detection buffer. Following overnight incubation at RT, 80 μ l of medium was removed from each well before reading the 96-well plates a PHERAstar by measuring the signals of the donor (Eu cryptate-labeled AP2 antibody) at a wavelength of 620 nm, and of the acceptor at 665 nm (d2-labeled β Arr2). Finally, the results were expressed as the FRET ratio $[(665/620) \times 10,000]$ and plotted using GraphPad 9.1.1 (GraphPad Prism software inc.). Experiments were repeated at least three times on different cultures, each condition in triplicate. Data are presented as means \pm SEM.

2.11. Enhanced bystander bioluminescence resonance energy transfer (BRET) β arr recruitment assay

β arrs recruitment to ligand-activated GPCRs using an enhanced bystander BRET (ebBRET) assay has been previously described [67]. The assay is based on measuring β arr1 or β arr2 translocation from the cytoplasm to the plasma membrane upon GPCR activation, using a *Renilla* Luciferase II fused to β arr1 or 2 (BRET donors) and a CAAX prenylation motif from the K-RAS protein fused to the C-terminus of *Renilla* GFP (BRET acceptor) which anchors GFP at the plasma membrane. Here, the β arr1-RlucII or β arr2-RlucII [68] recruitment to activated V2R at the plasma membrane results in an increase in BRET signal. Briefly, 35000 cells in 100 μ l DMEM were transfected with 100 ng of total DNA (10 μ l NaCl 150 mM containing 5 ng of pRK5-SNAPtag-V2R, 5 ng of either pcDNA3.1- β arr1-RlucII or pcDNA3.1- β arr2-RlucII, 30 ng of pcDNA3.1-rGFP-CAAX and 60 ng of salmon sperm DNA (ThermoFisher)) using transfecting agent polyethylenimine (PEI linear, MW 25KTM, 1 mg/ml, Polysciences) at a ratio of 0.3 μ l PEI per 100 ng DNA. Transfected cells were plated in poly-L-ornithine-precoated white-walled, flat-bottom, 96-well plates (Greiner CELLSTAR plate, Sigma-Aldrich). After a 48-hour culture period, cells were rinsed once with 100 μ l per well of PBS and incubated 30 min at 37 °C with 80 μ l per well of Tyrode Buffer (137 mM NaCl, 0.9 mM KCl, 1 mM MgCl₂, 1.9 mM NaHCO₃, 3.6 mM NaH₂PO₄, 25 mM HEPES, 5.5 mM Glucose, and 1 mM CaCl₂, pH 7.4). Cells were treated for the last 5 min with the ligands (final concentration from 10^{-11} to 10^{-5} M, diluted in Tyrode buffer) and the Luciferase substrate (2.5 μ M methoxy e-Coelenterazine (NanoLight), diluted in Tyrode buffer). ebBRET was then measured between RlucII (BRET donor)- and rGFP (BRET acceptor)-tagged proteins. BRET values were obtained from a single 1 s time period measurement in each well using a MithrasTM LB940 Multimode Microplate Reader (Berthold Technologies, Germany) to generate concentration–response curves, and were obtained by calculating the ratio of the light emitted by the energy acceptor over the light emitted by the energy donor (acceptor 515 nm/donor 410 nm). Data were collected using the MicroWin 2000 software (Berthold Technologies, Germany), and were analyzed with GraphPad Prism v 9.1.1 (GraphPad Prism Software Inc.) using the “dose-response stimulation” subroutine. Median effective concentrations were determined using the log(agonist) versus response fixed slope (three parameters) fit procedure. Experiments were repeated at least three times on different cultures, each condition in triplicate. Data are presented as means \pm SEM.

3. Results

3.1. NMR sensors and paramagnetic ligands

To characterize the conformational changes of V2R, we first introduced NMR sensors by methylating its lysines with two ¹³CH₃ groups for heteronuclear 1H-¹³C NMR [58,59]. The V2R construct has only

three lysines, K100^{2.65}, K116^{3.29} and K268^{6.32} (Fig. 1A and S1A). K100^{2.65} lies on the rim of the orthosteric pocket, whereas K116^{3.29} is located within the pocket. K268^{6.32} belongs to the cytoplasmic extremity of TM6, which potentially makes it an appropriate sensor of canonical activation, considering the pivotal role of TM6 therein [8,9,36–38]. Peak assignment of the heteronuclear 1H-¹³C HMQC spectrum of methylated V2R (Fig. 1B) was obtained by site-directed mutagenesis of lysines into arginines (Fig. S4).

Contrary to K100^{2.65} and K116^{3.29}, which have only one correlation peak, K268^{6.32} is represented by a major broad peak and at least one minor peak at a timescale around and above the microsecond range. NMR and mass spectrometry (MS) data eliminated the possibility of incomplete methylation labeling of lysine residues that may have resulted into several resonances for K268^{6.32} (Fig. S5A–B). Hence, the presence of a broad peak and a minor peak suggests the existence of several conformational states in the apo form, in an intermediate (major) and slow (minor) exchange at the NMR scale.

Secondly, we used ligand paramagnetic tagging on the agonists to help verify the ligand binding poses predicted by MD simulations. While the AVP binding pose was known, those of MCF14 and TVP are not. A carboxyl-PROXYL group, containing a nitroxide probe, was linked to either MCF14 or to the deaminated lysine-vasopressin (dLVP) to obtain their paramagnetic forms (^{par}MCF14 and ^{par}dLVP, respectively) (Fig. 1C, S1B, S3). dLVP is an AVP analog with the same activity toward V2R [69] and was used to facilitate chemical synthesis. The paramagnetic tag position in ^{par}MCF14 was determined based on the predicted binding pose. Since TVP-like V2R ligands bind mostly in E-aS-5(R/S) configurations [70], we chose the C5 position to insert a linker (Fig. 1C) in order to orient the paramagnetic nitroxide probe outward from the pocket. Introduction of the paramagnetic tag did not alter the signaling profiles of the ligands in terms of efficacy, although their affinity and potency were reduced (Fig. 2A, Table 1). ^{par}dLVP remains a full and unbiased agonist, whereas ^{par}MCF14 is a Gs-biased partial agonist unable to recruit β Arrs like its parent compound MCF14 (Figs. 1D, 2A, S6, Table S1).

3.2. Ligand binding pose validation by NMR and site-directed mutagenesis

Combining labeling of V2R and ligands, we used PREs of the ¹H nuclei to compare distances between the carboxyl-PROXYL group and the methyl groups of K100^{2.65} and K116^{3.29} lysines, while the corresponding distances were measured from the MD simulations. The PREs were estimated by comparing the volumes of the V2R lysine correlation peaks when the labeled V2R is in complex with the tagged ligands, in the paramagnetic and diamagnetic states (Fig. 2B). We used V2R^{K268R} for this purpose, to simplify the NMR spectra. The K268^{6.32}R mutation had negligible impacts on the ligand affinities and PREs compared to the WT receptor (Fig. 2A, S7A, Table S2). Addition of the paramagnetic ligands induced a decrease in the peak volumes of K100^{2.65} and K116^{3.29} (Figure S7B), due to the distance-dependent relaxation effects of the unpaired ion in the PROXYL and the ligand-induced conformational changes. Addition of 5 equivalents of the reducing agent ascorbic acid attenuated the paramagnetic interactions, resulting in an increase in the lysine peak volumes (peak fitting is illustrated in Figure S7B). The attenuation of the paramagnetic effect was stronger on K100^{2.65} than K116^{3.29} for both ^{par}dLVP and ^{par}MCF14, suggesting that the side-chain methyls of K100^{2.65} are closer to the paramagnetic center than those of K116^{3.29} (Fig. 2B). We then investigated if these results were retrieved in the MD simulations.

^{par}dLVP maintained the same binding pose as AVP observed in the cryo-EM structures (Fig. 2C, S8) [36–39]. The paramagnetic tag swayed at the entrance of the orthosteric pocket (Fig. 2C), resulting in multimodal probability distributions of the distances between the nitroxide ion and K100^{2.65}/K116^{3.29} methyl groups (Fig. 2D). The distance to K100^{2.65} was shorter than that to K116^{3.29} (Fig. 2D, S9). We then inves-

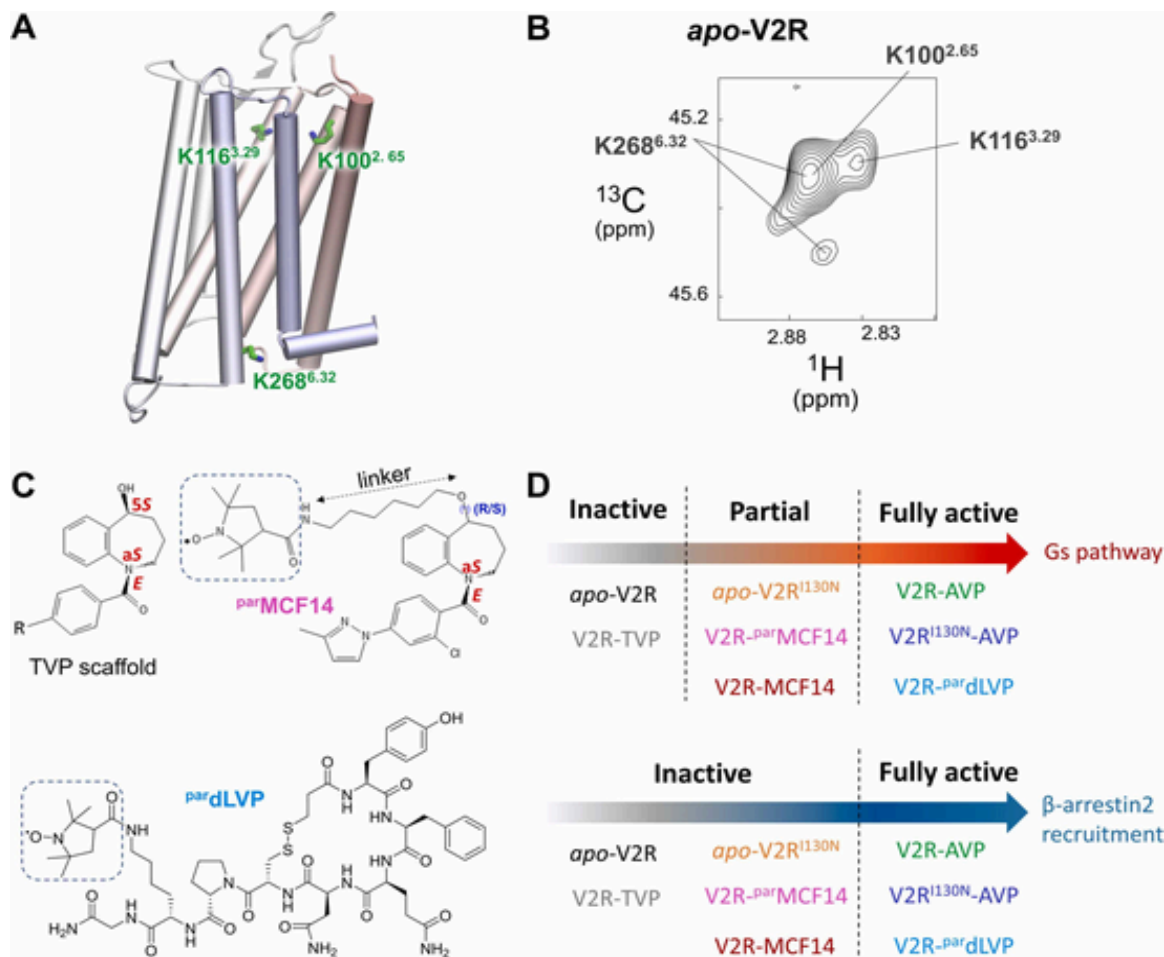


Fig. 1. NMR probes, paramagnetic labels, and functional profiles of the systems studied. (A) Position of the three lysine sensors in inactive V2R. (B) ^1H - ^{13}C HMQC NMR spectrum of $^{13}\text{CH}_3$ -Lys-V2R. (C) Stereochemical configuration of TVP-type V2R ligands and chemical structures of the paramagnetic agonists (see also Fig. S1B). The paramagnetic tags are boxed. The chiral center of $^{\text{par}}\text{MCF14}$ is marked. (D) Functional profile of all systems studied in the MD simulations (see also Table S1).

titigated the binding pose of TVP and TVP analogs using the same MD simulation protocol. It has been shown that TVP analogs bind V2R in the *E*-aS configuration (Fig. 1C, S1) [70], which was used here. Their *endo* isomer (Figure S1B) was found to be more stable in the binding pocket. $^{\text{par}}\text{MCF14}$ and TVP can also be a mixture of two enantiomer 5 R/S (Fig. 1C, S1). R- $^{\text{par}}\text{MCF14}$ turned out to be highly mobile in the pocket during the simulations (Figure S8). This is consistent with the fact that V2R favors the S-configuration of TVP-type ligands [70]. S- $^{\text{par}}\text{MCF14}$ was stable in the pocket and adopted the same binding pose as the untagged MCF14 (Fig. 2C, S8). Therefore, R- $^{\text{par}}\text{MCF14}$ was discarded to facilitate the discussion, and hereafter we refer to S- $^{\text{par}}\text{MCF14}$ as $^{\text{par}}\text{MCF14}$. The paramagnetic tag was also highly mobile in $^{\text{par}}\text{MCF14}$, where its nitroxide ion was closer to K100^{2.65} than K116^{3.29} (Fig. 2D and S9).

Both $^{\text{par}}\text{dLVP}$ and $^{\text{par}}\text{MCF14}$ were slightly more mobile than their untagged counterparts during the simulations (Figure S8), in accordance with their lower affinity determined in the cell assays. For both ligands, the paramagnetic center was closer to the K100^{2.65} methyl groups than those of K116^{3.29} (Fig. 2D and S9), in line with the stronger PREs estimated for K100^{2.65} (Fig. 2B). These results, along with the fact that the tagged ligands were fully functional in cell assays, support the predicted binding pose of MCF14 and TVP. Indeed, alternative binding poses would lead to stereo clashes of the tag in $^{\text{par}}\text{MCF14}$ with V2R. Finally, we studied the *E*-5R and *E*-5S configurations of TVP, which

turned out to bind equally stable in the pocket, yet their binding poses were slightly different (Fig. 3A, S8 and S10). The predicted TVP binding mode is in line with sited-directed mutagenesis data from the literature by Liu *et al.* [71]. Nevertheless, Liu *et al.* proposed two alternative binding orientations for TVP. To validate the putative binding mode of TVP and MCF14, we performed site-directed mutagenesis of ligand-binding residues, in combination with TR-FRET binding affinity measurements for TVP, MCF14 and AVP (the latter being a reference with a known binding mode [36]) (Fig. 4). First, we ensured that all transiently transfected variant receptors displayed a comparable cell surface level of expression to that of the WT (Fig. 4A). The affinity (*K*_d in nM) of the fluorescent benzazepine-red (a V2R antagonist and TVP analog, as a reference tracer) for each mutant was then calculated using saturation TR-FRET binding assays. Finally, AVP, TVP and MCF14 affinity (*K*_i in nM) for the mutants were measured by competition against benzazepine-red. The F178A completely abolished benzazepine-red binding (Fig. 4B), preventing the affinity calculation for TVP, MCF14, and AVP in this mutant. M120A and Q174A also significantly decreased the benzazepine-red binding affinity. These indicate that F178, M120 and Q174 are critical for the binding of the benzazepine scaffold (characteristic for TVP-type ligands). Indeed, Q174A drastically reduced the affinity of all the ligands, revealing a central role of this residue in the binding pocket (Fig. 4C-E and S10). Some mutations differentially affected the affinity of these ligands, suggesting that these residues contribute to

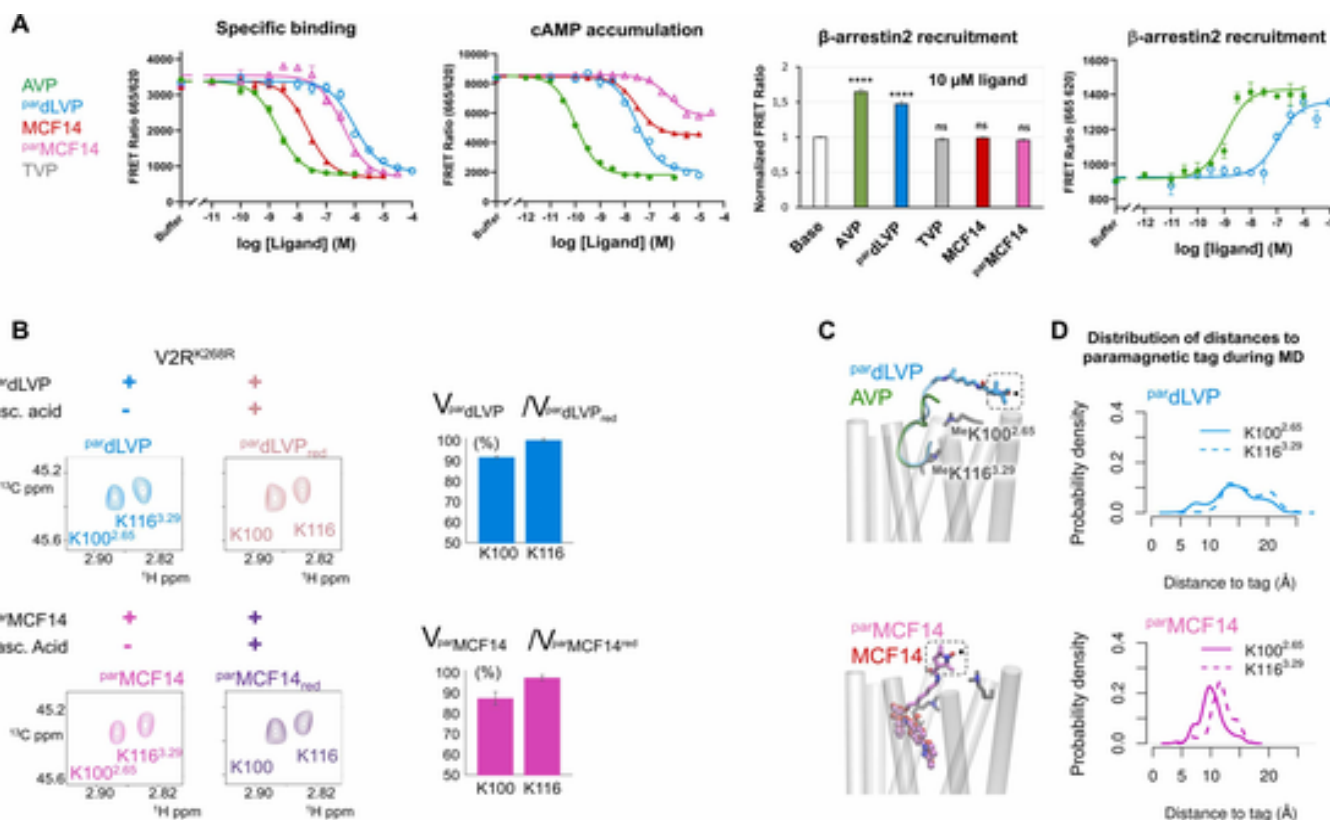


Fig. 2. Pharmacological properties and binding poses of the ligands in V2R. (A) Binding properties (left), effects on cAMP accumulation (central-left) and β arr2 recruitment (center-right and right). TR-FRET was expressed as FRET ratio (665 nm/620 nm x 10,000). * * * *, $p < 0.0001$; ns, not significant ($p > 0.05$). (B) Extracted HMQC spectra of K100^{2.65} and K116^{3.29} resonances of V2R K268^{5.32}R bound to 665 dLVP (sky blue) or 665 MCF14 (magenta), and reduced by ascorbic acid (mauve taupe and light violet, respectively). Ratios of peak volumes in the paramagnetic and diamagnetic (ligand_{red}) forms of each agonist are shown to the right. Volumes were quantitated using the nlinLS subroutine of NMRpipe (Fig. S7B).[62] They identify K100^{2.65} methyl groups as the closest to the nitroxide ion. Error bars come from two experiments recorded with the receptor purified from two different batches. (C) Snapshots of tagged and non-tagged agonists during MD simulations. The nitroxide cage is squared. Tagged and non-tagged agonists showed identical binding poses in the pocket, while the tag and linker swayed around the entrance of the pocket. (D) Probability density distribution of the distances between the PROXYL nitroxide ion and the methyl groups of K100^{2.65} (plain line) and K116^{3.32} (dashed line) during the MD simulations. Due to inherent inaccuracies in the simulations, the values may not be quantitatively interpreted for comparison with the NMR data. They illustrate a qualitative trend that aligns with the NMR spectra.

Table 1

Ligand affinity and potency in living cells^a.

Ki (nM) ^b	EC50 (nM) ^b	
	cAMP	β Arr2
AVP	0.93 ± 0.3 (n = 5)	0.11 ± 0.01
665 dLVP	273.5 ± 39.7	37.5 ± 3.2
MCF14	7.9 ± 2.3	40.9 ± 11.6
665 MCF14	169.7 ± 24.7	647.6 ± 37 (n = 5)

^a Measured in cells expressing the V2R construct used for NMR (Fig. S1A).

^b Values are mean ± SEM (n = 3, unless otherwise indicated).

^c n.a. = not applicable.

subtle differences in the binding mode of the TVP analogs. Namely, Q92A and M120A significantly decreased the affinity for AVP and benzazepine-red but increased that of MCF14, with no effect on TVP. F287A reduced AVP and TVP affinity, with no effect on MCF14 and benzazepine-red. These results demonstrated a critical role of Q174 and F178 in MCF14 and TVP binding. Indeed, Q174 forms an H-bond with both ligands in the MD simulations, whereas F178 acts as a hydrophobic cap of the binding pocket (Fig. 3A and S10). Q92A, M120A and F287A showed varying effects on MCF14 and TVP, aligning with the MD predictions that these residues directly interact with the distinct regions of the two ligands (Fig. 3A). In summary, site-directed mutagenesis

data from the literature [71] and our assays strongly substantiate the binding modes of TVP and MCF14 obtained from the MD simulations.

3.3. Correlation of V2R conformational changes with ligand and mutation signaling profiles

Having determined the ligand binding poses, we investigated the structural features associated with V2R activation by solution NMR and MD simulations. Among the eight simulation systems studied (Fig. 1D, Table S1), we included the I130^{3.43}N mutant, which was previously described to constitutively activate the Gs pathway, but not the β Arr one [33], consistent with our assay outcome (Figure S11). Upon AVP stimulation, the mutant could activate both Gs and β Arr pathways, indicating that AVP overrides the mutational effect on the signaling preference. Therefore, the eight systems divide into three categories: inactive, biased Gs (partial or not) activation, and unbiased activation (Fig. 1D, Table S1).

All six systems in the activation category showed apparent TM6 outward movements on the cytoplasmic side in the MD simulations (Fig. 3A, S12, S13A, S14). V2R-AVP exhibited the highest flexibility and distinct conformational clusters at the intracellular end of TM6. Interestingly, E-5R-TVP stabilized TM6 in the initial position with a TM2-TM6 distance unchanged, like apo-V2R, whereas E-5S-TVP induced further closure of TM6. Moreover, E-5S-TVP induced distinct orientations of

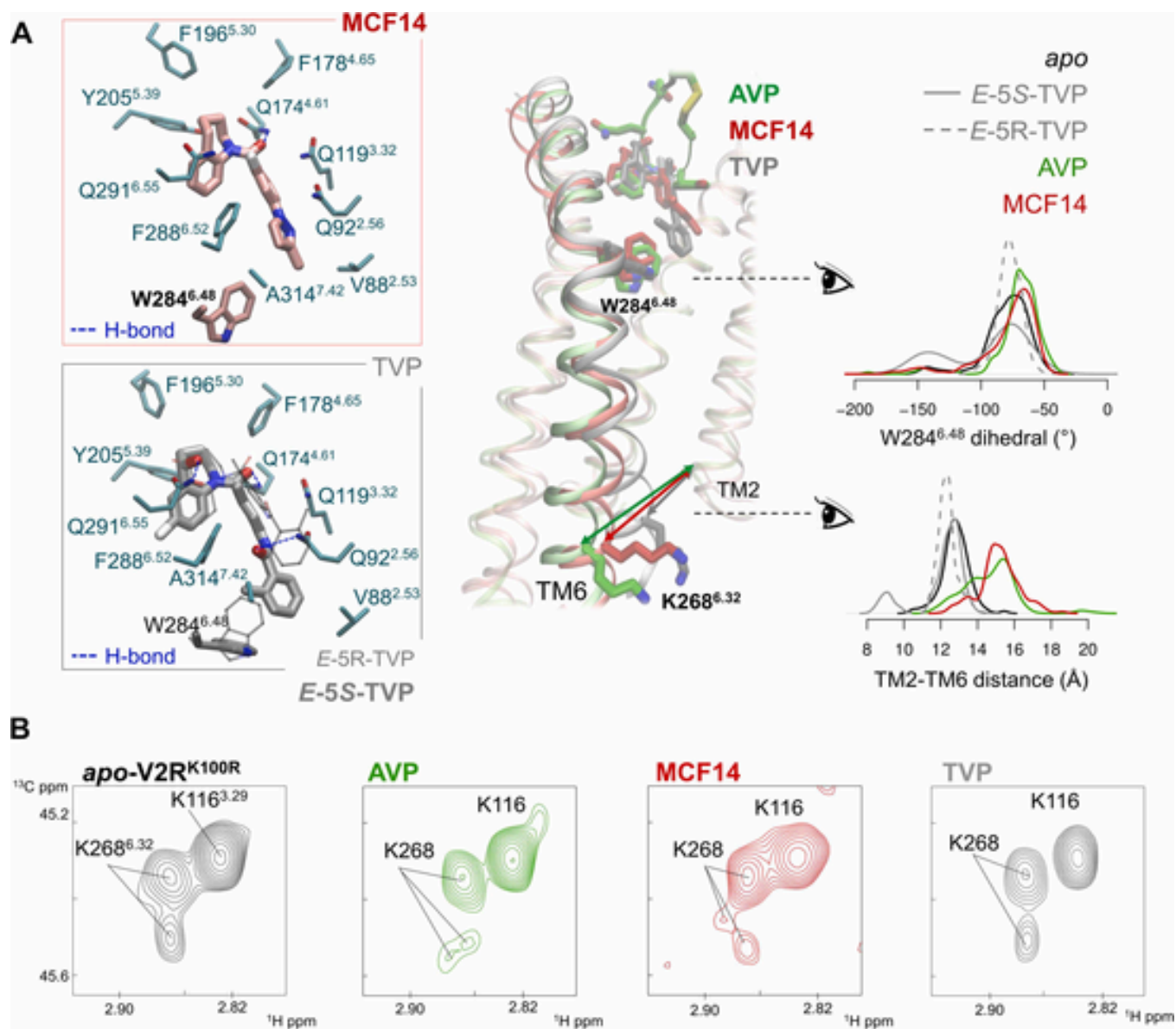


Fig. 3. Ligand-induced V2R conformational changes in TM6. (A) MD simulations showed that MCF14 and TVP adopted similar binding poses. Residues within 3 Å distance of the ligands are shown in sticks. The binding poses of *E*-5S-TVP and *E*-5R-TVP are shown in sticks and lines, respectively. TVP altered the side-chain orientation of W284^{6.48}, and TM6 remained in the initial position close to TM2 on the intracellular side. MCF14 (biased agonist) and AVP (unbiased agonist) stabilized the same W284^{6.48} sidechain orientation (dihedral angle χ_2 around -70°) and led to TM6 opening on the intracellular side. TM2-TM6 distance was measured by the center-of-mass distance between the backbones of I74^{2.39}-F77^{2.42} and V266^{6.30}-T269^{6.33}. Right panel shows the density distribution of W284^{6.48} side-chain dihedral angle χ_2 and the TM2-TM6 distance during the MD simulations. (B) HMQC spectra of the K100^{2.65}R mutant in *apo* form (black) and in the presence of an excess of AVP (green), MCF14 (red) and TVP (gray). Spectra represented in (B) were recorded on samples originating from the same batch of V2R purification, except for TVP, whose reference spectrum is shown in Fig. S15B.

W284^{6.48} side-chain contrasting all the other seven systems (Fig. 3A, S13A). These data suggest stronger inhibition by *E*-5S-TVP than *E*-5R-TVP for V2R, consistent with the previous study of TVP analogs [70]. W284^{6.48} is part of the conserved CW^{6.48}xP motif in class A GPCRs, known as the “toggle switch” of receptor activation [7,22]. Therefore, TVP likely antagonizes V2R by blocking this activation switch through its *E*-5S configuration.

The conformational dynamics observed in the MD simulations were experimentally investigated by measuring the changes in the NMR correlation peaks of V2R lysines, with a focus on K268^{6.32}. Indeed, to observe clear signals, we used the V2R^{K100R} mutant that preserves the signaling properties of WT V2R (Figure S15 A, Table S3). In its *apo* form, K268^{6.32} showed at least two resonance peaks, the main peak being also

large and indicative of conformational heterogeneity at TM6 intracellular extremity (Fig. 3B). Binding of the antagonist TVP caused no significant change, except a narrowing of peaks, indicating that the *apo* form was mainly in an inactive state, stabilized by TVP (Figure S15B). The minor peak was observed only in the *apo*- and the TVP-bound states, suggesting that it is characteristic of them. Binding of AVP indeed resulted in a narrowing of the K116^{3.29} and K268^{6.32} major peaks, while the K268^{6.32} minor peak (at 2.86/45.2 ppm) was split into two components of equal but weaker intensities (Fig. 3B). In the case of MCF14, binding caused an increase in the line widths of the V2R K268^{6.32} and K116^{3.29} major peaks, together with an increase of 20 % in the peak intensity of K268^{6.32} (Fig. 3B, S15C). As with AVP, the smallest peak of K268^{6.32} was also split into two peaks of unequal intensities but at dif-

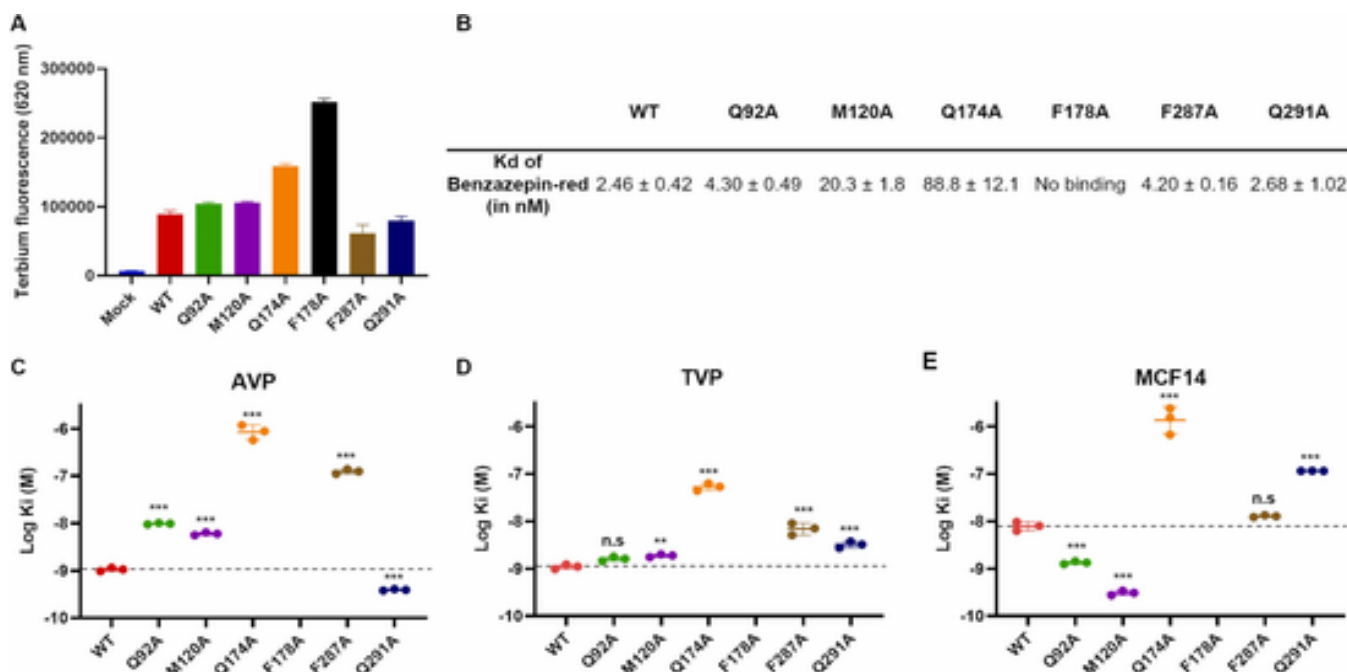


Fig. 4. Effect of site-directed mutagenesis of key V2R residues on AVP, TVP and MCF14 binding affinity. (A) Cell surface expression level of V2R WT and mutants measured using the terbium donor fluorescence following cell labeling. Although the level of expression does not affect the calculated K_i values, quantity of the plasmids coding for each construct was optimized to obtain equivalent receptor expression levels. (B) Affinity (Kd) of the fluorescent benzazepine-red tracer was calculated from saturation binding experiments. (C-E) Affinity (K_i) of AVP, TVP and MCF14 was calculated from competition binding experiments using the benzazepine-red as a tracer. Dashed lines indicate the mean K_i of each ligand for the WT. Data are mean \pm SEM from 3 to 6 individual experiments each performed in triplicates. Statistical significance was assessed using one-way ANOVA, comparing all mutants to the WT. * ** : $p < 0.001$; * : $p < 0.01$ and n.s: not significant.

ferent chemical shifts, one being close to the small peak found in the inactive states (2.86/45.2 ppm).

Hence, altogether, NMR spectra suggest that both AVP and MCF14 propagate different conformational dynamics to TM6 cytoplasmic extremity. Other receptors bound to an agonist alone (without intracellular transducers) have been reported to be structurally heterogeneous, with a high proportion of inactive states [72–74]. Notably, our cryo-EM analysis of V2R complexed with AVP and Gs allowed to generate three maps with distinct conformations [36]. It suggests that agonist-bound V2R exist in at least three distinct states that differ in Gs protein engagement and in the capacities of nucleotide exchange.

3.4. Biased activation mechanism

Comparing V2R-MCF14 and V2R-AVP in the MD simulations, we observed different conformations in TM7 and H8 (Fig. 5A). TM7-H8 were also less dynamic in V2R-MCF14. This is illustrated by the narrower distributions of the interhelical distances in V2R-MCF14 (TM2-TM7, TM1-TM7 and TM1-H8, Fig. 5A). MCF14 led to inward movements of TM7 from the pocket to the NP^{7.50}xxY motif, where Y325^{7.53} formed contacts (water-mediated or direct H-bonds) with T134^{3.47} in TM3. This likely restrained TM7 and H8. As a result, H8 was closer to TM1 than in V2R-AVP (Fig. 5A, R67^{1.62}-S331^{8.49} distance). ^{par}MCF14 had similar effects on the TM7-H8 dynamics, except for larger fluctuations in the orthosteric pocket due to its lower affinity (Figures S13B, S14). This was not the case for TVP, despite its chemical similarity to MCF14 (Figure S12B). Therefore, the above differences between V2R-MCF14 and V2R-AVP are likely linked to differences in the activation process and the chemical structures of the ligands.

To verify whether MCF14 indeed alters the conformational dynamics in NP^{7.50}xxY and H8, we introduced a lysine probe in TM1 by mutating R64^{1.59} into a lysine. This position was chosen because R64^{1.59} was the reference point for measuring the NP^{7.50}xxY-H8 dynamics in the

MD simulations (Fig. 5A). To minimize spectral crowding, we used the double mutant R64^{1.59}K/K100^{2.65}R and assigned the NMR correlation peak of K64^{1.59} by comparison with the spectrum of V2R^{K100R} (Figure S16). The K64^{1.59} peak was indeed different in the MCF14-bound state, whereas in the AVP-bound state, it resembled the *apo* state (Fig. 5B). This supports the MD predictions and substantiates the hypothesis that the NP^{7.50}xxY-H8 dynamics contribute to activation bias (Fig. 5A).

Remarkably, the I130^{3.43}N mutation led to similar conformations at NP^{7.50}xxY and H8 compared to V2R-MCF14 (Fig. 6A, S13B, S14). The mutation also generated additional H-bonds between TM3 and NP^{7.50}xxY, leading to inward movements of TM7-H8. While the effect of MCF14 seemed allosteric, propagating from the orthosteric pocket to the intracellular side, the effect of I130^{3.43}N was more local, restraining NP^{7.50}xxY through direct H-bonds. Indeed, *apo*-V2R^{I130N} showed different conformations in the orthosteric pocket than V2R-MCF14 (Fig. 6A). Interestingly, AVP binding could counteract the effect of I130^{3.43}N and destabilize the H-bonds between N130^{3.43} and NP^{7.50}xxY (Fig. 6B). AVP-bound V2R^{I130N} mutant (AVP-V2R^{I130N}) partially recovered the dynamics of NP^{7.50}xxY and H8 seen in WT V2R-AVP (Fig. 5A versus Fig. 6B). This is consistent with the experimental data that the I130^{3.43}N mutant could indeed recruit β Arr2 upon AVP stimulation (Figure S11). Therefore, the distinct NP^{7.50}xxY-H8 conformations found in V2R-MCF14 and *apo*-V2R^{I130N} are likely linked to their lack of β Arr2 signaling, contrasting V2R-AVP and V2R^{I130N}-AVP. Unfortunately, we could not record high-quality NMR spectra for this mutant, which showed a degraded migration profile in SDS gels and could not be concentrated, even starting from 24 L of culture. However, our results suggest that the mutant V2R^{I130N} adopts a conformation similar to that of V2R-MCF14 and is unable to trigger detectable β Arr signaling. This conformation is clearly different from that triggered by the binding of AVP to WT and mutant receptors. Thus, we assume existence of two distinct interconnected conformations which differ in the outcome of signaling.

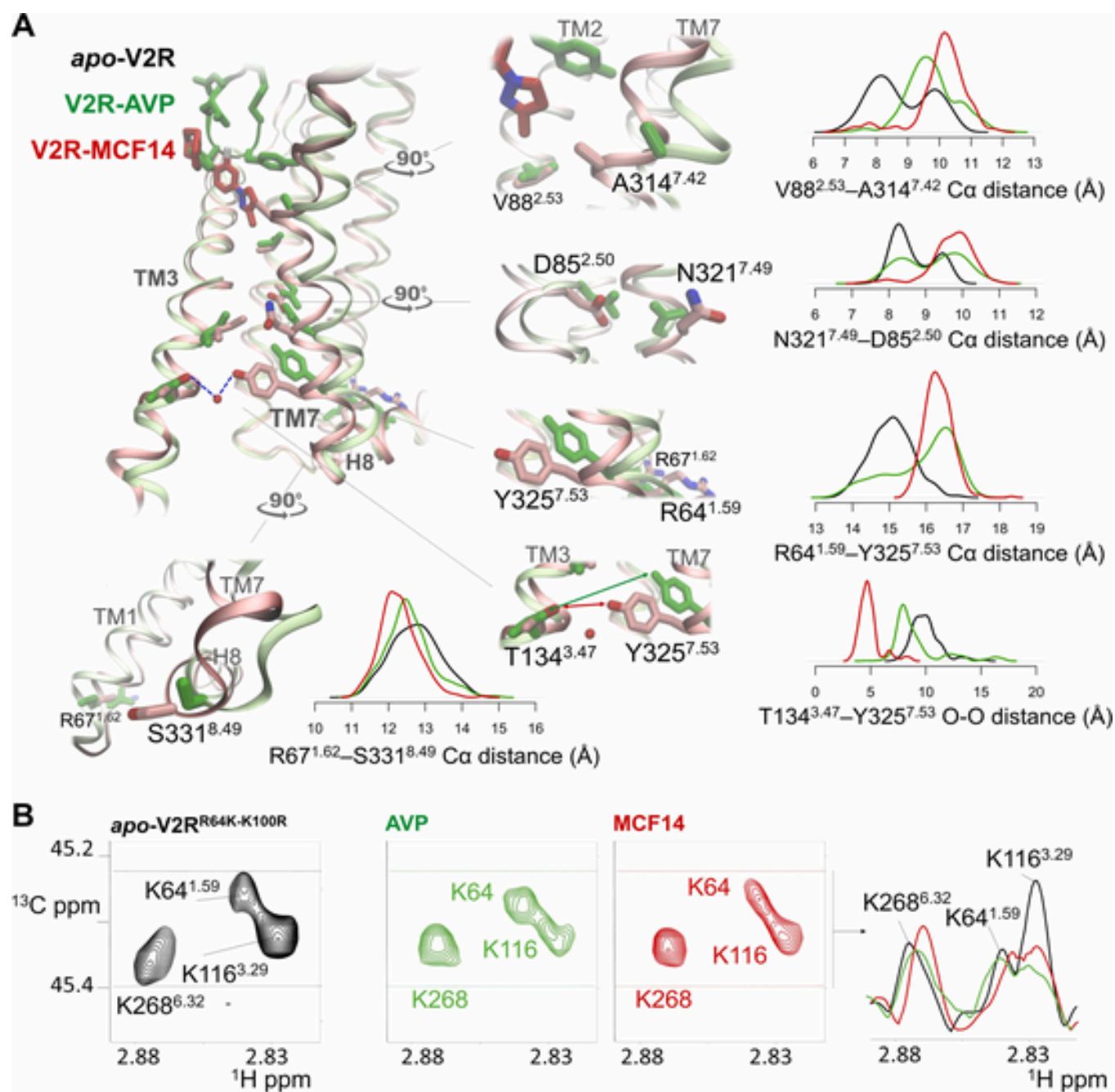


Fig. 5. Changes in TM7 and H8 conformational dynamics induced by MCF14 and AVP. (A) MCF14 lead to inward displacements of TM7, which propagated from the binding site to the NP^{7.50}_{xx}Y^{7.53} motif. A series of intrahelical distances were measured to illustrate the TM7-H8 dynamics in *apo*-V2R (black), V2R-AVP (green) and V2R-MCF14 (red). Probability density distribution plots of the distances show that in V2R-MCF14, TM7 was less dynamic and moved inward, away from TM1-TM2. On the intracellular side, Y325^{7.53} formed direct or water-mediated H-bonds with T134^{3.47}, anchoring the N^{7.49} PxxY^{7.53} motif to TM3. As a result, TM7 movements were restrained and H8 was closer to TM1 than in V2R-AVP or *apo*-V2R. (B) Spectral signature of ligand impact on the K64^{1.59} NMR probe. 1D spectra on the right correspond to 1D projections along the ¹³C dimension between the two dashed lines. The intracellular extremity of TM1 experiences a different environment according to the ligand pharmacological profile. The ¹H dimension of K64 resonance in the AVP-bound state retains a component similar to the apo state at 2.84 ppm, contrary to MCF14-V2R. Proton chemical shifts reflect changes in the structural environment whereas the ¹³C indirect dimension is more sensitive to local dihedral angles.

4. Discussion and conclusion

Biased signaling has raised tremendous interest over the last decade, because it holds the promise of more specific drugs with fewer side-effects. This phenomenon occurs via ligand-dependent mechanisms or mutations altering the conformational equilibrium of GPCRs. While the TM6 displacement is a reference marker for receptor activation, the

present study indicates that TM7-H8 conformational changes are likely associated with biased signaling (Figs. 5, 6). Using V2R as a prototypical system, our enhanced-sampling MD simulations provided detailed description of the ligand binding poses and receptor dynamics, validated by site-directed mutagenesis, functional assays and NMR spectra. In our study, the eight V2R systems displayed varying dynamics in TM6, TM7 and H8 on the receptor intracellular side (Figure S14). In

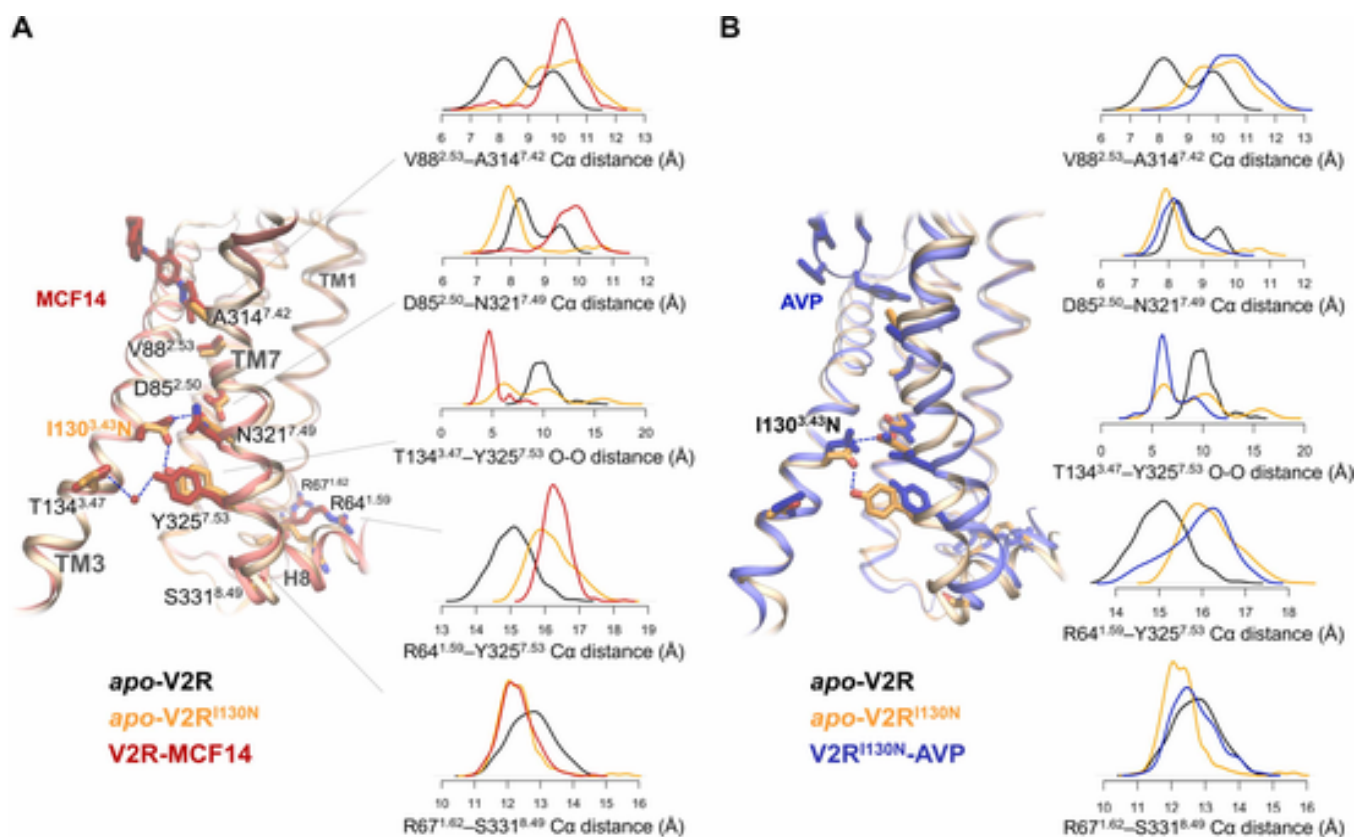


Fig. 6. Mutation I130^{3.43}N and MCF14 induced similar conformational changes in N^{7.49}PxxY^{7.53} and H8, contrasting with AVP. (A) I130^{3.43}N mutation and MCF14 both led to H-bonds between TM3 and the NPxxY motif, restraining the dynamics of the latter. This resulted in the same H8 position relative to TM1, which is more compact than that in *apo*-V2R (black). I130^{3.43}N altered the NPxxY conformations by direct H-bonds, whereas MCF14 had long-range allosteric effects. The *apo*-V2R^{I130N} showed different TM7 conformations near the orthosteric pocket and Na⁺-binding site (the conserved D85^{2.50}) than V2R-MCF14 (B) Comparing *apo*-V2R and AVP-bound (blue) V2R^{I130N} mutant, AVP appeared to counteract the effect of I130^{3.43}N and undermine the N130^{3.43}-NPxxY H-bonds. In AVP-V2R^{I130N}, NPxxY and H8 recovered the dynamics that resembled that in WT V2R-AVP (Fig. 5A).

particular, we identified distinct receptor conformations in the TM7 NP^{7.50}xxY motif and H8, induced by the Gs-biased MCF14 ligand and the Gs-biased I130N mutation. Although we cannot formally exclude that these particular conformations may also contribute to the partial agonist nature of MCF14, the striking similarity between the ligand- and the mutation-induced Gs-activation modes highlights the likelihood of pathway selectivity rather than partial activation. Our results are in line with our previous findings using fluorescent probes introduced in V2R TM6 and at the TM7-H8 junction [12]. The present work provides however a far more comprehensive and detailed mechanistic view, encapsulated in the schematic illustration of Fig. 7. In our model, we hypothesize that the biased agonist MCF14 induces these conformational changes allosterically, through the conserved Na⁺-binding site in TM2 (D85^{2.50}) and the NP^{7.50}xxY motif in TM7. The I130^{3.43}N mutation, however, seems to directly act on the NP^{7.50}xxY motif, resulting in similar NP^{7.50}xxY-H8 conformations to those in V2R-MCF14. Similar patterns at TM7-H8 associated with G_i protein bias have been observed in the μ - and κ -opioid receptors [13,75].

It is worth noting that the comparisons between the NMR and the MD data in this work are qualitative. This is partially due to inherent inaccuracies and insufficient sampling of the simulations but also of the methodology used. Despite the state-of-the-art enhanced-sampling technique used, the MD simulations may not capture the slow exchanges in the NMR data. The NMR study was performed using LMNG as a detergent (supplemented with CHS), whereas the MD simulations used a bilayer lipid environment. LMNG (in combination with CHS) is considered as one of the best detergents in terms of preserving function-

ality of purified GPCRs [14,76,77] and has been shown to not alter the biased signaling properties of GPCRs. Indeed, structures of the GLP-1 receptor/Gs protein complex bound to the unbiased peptide GLP-1 or the biased agonist exendin-P5 were solved and compared, the two complexes being prepared in LMNG/CHS detergent micelles [78,79]. These results show that LMNG/CHS micelles can be used to study different active conformations of a given GPCR. We also used sub-stoichiometry of paramagnetic ligands to avoid non-specific binding and PREs, but cannot exclude that they partition in empty LMNG micelles, further lowering their apparent final concentration. Finally, due the low concentration of the NMR sample (30 μ M), we could not resort to optimized pulse sequences designed to precisely measure PREs [80].

Residue I130^{3.43} may play a particular role in GPCR activation and biased signaling. This largely conserved residue [81] restrains the inactive state of several receptors [3,82,83]. A systematic mutational investigation of the melanocortin 4 receptor indicated its role in signaling bias [84]. We show here that the I130^{3.43}N mutation in V2R led to constitutive cAMP signaling without β Arr2 recruitment, in line with previous reports [33]. By contrast, upon AVP stimulation, the V2R^{I130N} variant displayed a higher β Arr2 recruitment level than WT-V2R (Figure S11), suggesting a particular role of residue I130^{3.43} for β Arr2 signaling mediated by its direct interactions with the NP^{7.50}xxY motif in TM7.

Switching GPCR signaling between G protein to β Arr pathways depends on the binding and activation of GRKs (reviewed in [85]). These kinases, like G proteins and β Arrs, also bind to the cytoplasmic cavity of activated GPCRs as shown for GRK2 into the neurotensin receptor NTSR1 open pocket [86], and for GRK1 into the activated rhodopsin

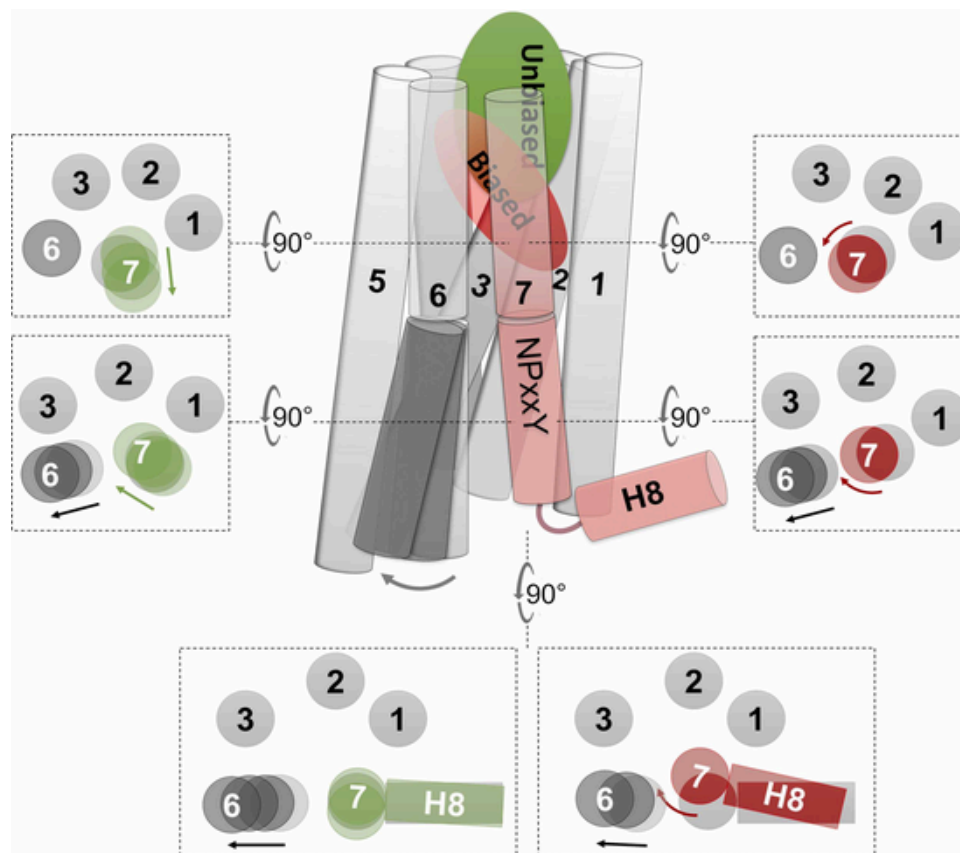


Fig. 7. Proposed scheme of V2R conformational changes associated with G protein-biased and unbiased agonists. Both types of agonists trigger TM6 opening on the intracellular side. The G protein-biased agonist (red) restricts TM7 at the orthosteric pocket, inducing the N^{7,49} PxxY^{7,53} motif to shift toward TM3 and drawing H8 closer to TM1. Unbiased agonist (green) does not trigger this structural limitation, leading to both G protein- and β Arr protein-associated signaling pathways.

[87]. According to our MD simulations, MCF14 binding and the I130^{3,43}N mutation led to TM7-H8 movements toward TM1 and TM3, resulting in a more compact intracellular binding pocket of V2R. This likely impedes or limits the insertion of the N-terminal helix of GRKs into V2R, and also prevents interactions of the β Arr finger loop (in the NTSR1-GRK2 and NTSR1-arrestin2 structures, the finger loop of β Arr and N-terminal helix of GKR2 overlap). The finger loop of β Arr1 indeed slots between residues A140^{3,53}-I141^{3,54} in TM3 and a cluster of Ser residues (S329^{8,47}-S330^{8,48}-S331^{8,49} at the TM7-H8 junction) [39]. Thus, conformations and dynamics of the receptor in the G protein biased state might be related to diminished GRK binding and receptor phosphorylation, and/or decreased β Arr recruitment. Moreover, the narrowing of the V2R receptor intracellular pocket by movements of TM7 to TM3 upon MCF14 binding may also limit insertion of Gs proteins and explain why this ligand is only a Gs protein partial agonist.

Increasing evidence points to the particular role of TM7 and H8 in the G protein/ β Arr bias of class A GPCRs. Some studies attributed ligand and bias to specific ligand-TM7 interactions [88–91]; others associated biased signaling to distinct conformations in the Na⁺-binding site, the NP^{7,50}xxY motif, as well as in the H8 [12,13,17,18,88,90,92–94]. In line with previous studies, our work on the V2R reaffirm the presence of a conserved mechanism associated with biased activation of class A GPCRs (Fig. 7). However, the detailed structural features may vary among different receptors, ligands and mutants. Nevertheless, analysis of receptor-ligand interactions and bias-associated receptor conformations can provide direct information for structure-based design of biased ligands [18,88,89,91,92]. Comparing the V2R conformations bound to AVP and MCF14, the major difference lies in the TM7 at both the orthosteric pocket and the intracellular side (Fig. 5A). Residue Y2 of

AVP forms major interactions with TM7, pushing it outward, which contrasts with the MCF14-bound form. Our data suggest that the TM7-inward conformation is associated with the lack of β Arr signaling. Therefore, the design of new Gs-biased V2R agonists may focus on the TM-inward conformation and avoid the sub-pocket occupied by AVP Y2.

Clinical translation of GPCR ligand bias is challenging due to the highly dynamic nature of GPCR activation. High-resolution structures of GPCRs bound to biased ligands have been reported, however, the mechanism of bias remains obscure since these are static snapshots stabilized by G proteins or nanobodies. The approach of combining NMR (or other relevant measurements of protein dynamics) with MD simulations offers a solution for deciphering the bias mechanism. Moreover, our findings indicate conserved structural patterns for G protein bias that may be common to other class A GPCRs. These will serve structure-based design of biased ligands in follow-up studies.

Author contributions

HD, BM, XC and DB designed the research; AF, PC, GG, BM, HO, XC, HD, CM, AK, RL, JN, SR, SU, and JD performed research; AF, PC, HO, BM, HD, DB, AK, SR, and XC analyzed data; HD, BM, XC, DB, AF, PC and GG wrote the original draft; AF, PC, GG, HO, XC, BM, HD, RS, SG edited the manuscript.

CRedit authorship contribution statement

Hélène Déméné : Writing – review & editing, Writing – original draft, Supervision, Project administration, Methodology, Investigation,

Funding acquisition, Formal analysis, Conceptualization. **Christiane Mendre**: Investigation. **Ali Kanso**: Investigation. **Xiaojing Cong**: Writing – review & editing, Writing – original draft, Investigation, Funding acquisition, Conceptualization. **Hélène Orcel**: Writing – review & editing, Investigation. **Bernard Mouillac**: Writing – review & editing, Writing – original draft, Supervision, Methodology, Investigation, Funding acquisition, Conceptualization. **Pierre Couvineau**: Writing – review & editing, Writing – original draft, Investigation. **Sébastien Granier**: Writing – review & editing. **Aurélien Fouillien**: Writing – review & editing, Writing – original draft, Investigation. **Dominique Bonnet**: Writing – review & editing, Writing – original draft, Supervision, Methodology. **Stéphanie Riché**: Investigation. **Remy Sounier**: Writing – review & editing, Methodology. **Gérald Gaibelet**: Writing – review & editing, Investigation. **Juliette Dimon**: Investigation. **Serge Urbach**: Writing – original draft, Investigation. **Romain Lanotte**: Investigation. **Julie Nguyen**: Investigation.

Declaration of Competing Interest

The authors declare no conflict of interest.

Acknowledgments

This work benefited from access to the NMR facilities of the Integrated Biophysics and Structural Biology Platform (PIBBS) of the CBS. PIBBS is a GIS-IBISA platform and belongs to the French Infrastructure for Integrated Structural Biology (FRISBI), supported by the National Research Agency (ANR-10-INBS-05) We thank the Institut de Génomique Fonctionnelle Arpege Pharmacology platform (<http://www.arpege.cnrs.fr>) for access to their instruments, and PerkinElmer Revvity for providing reagents. MS experiments were performed at the Montpellier Proteomics Platform (PPM, BioCampus Montpellier). This work was supported by grants from ANR (22-CE44-0021 to H. D. and B. M.), FRM (DEQ20150331736 to B. M. and EQU202203014649 to S.G.), and was also supported by the University of Strasbourg, the Interdisciplinary Thematic Institute IMS (ANR-10-IDEX-0002) and SFRI (STRAT'US project, ANR-20-SFRI-0012 to D.B.) under the framework of the French Investments for the Future Program. Core fundings were provided by CNRS, INSERM and Université de Montpellier. MD simulations were performed using HPC resources from GENCI-TGCC (grant 2021–2022 A0100712461 to X.C.).

Appendix A. Supporting information

Supplementary data associated with this article can be found in the online version at [doi:10.1016/j.csbj.2024.10.039](https://doi.org/10.1016/j.csbj.2024.10.039) .

References

- Wooten D, Christopoulos A, Marti-Solano M, Babu M.M, Sexton P.M. Mechanisms of signalling and biased agonism in G protein-coupled receptors. *Nat Rev Mol Cell Biol* 2018;19:638–53. <https://doi.org/10.1038/s41580-018-0049-3> .
- Kolb P, Kenakin T, Alexander S.P.H, Bermudez M, Bohn L.M, Breinholt C.S, et al. Community guidelines for GPCR ligand bias: IUPHAR review 32. *Br J Pharmacol* 2022;179:3651–74. <https://doi.org/10.1111/bph.15811> .
- Tao Y.X. Constitutive activation of G protein-coupled receptors and diseases: insights into mechanisms of activation and therapeutics. *Pharmacol Ther* 2008; 120:129–48. <https://doi.org/10.1016/j.pharmthera.2008.07.005>.
- Yang L.K, Hou Z.S, Tao Y.X. Biased signaling in naturally occurring mutations of G protein-coupled receptors associated with diverse human diseases. *Biochim Biophys Acta - Mol Basis Dis* 2021;1867:165973. <https://doi.org/10.1016/j.bbadis.2020.165973>.
- Venkatakrishnan A.J, Deupi X, Lebon G, Heydenreich F.M, Flock T, Miljus T, et al. Diverse activation pathways in class A GPCRs converge near the G-protein-coupling region. *Nat Publ Gr* 2016;536:484–7. <https://doi.org/10.1038/nature19107>.
- Zhou Q, Yang D, Wu M, Guo Y, Guo W, Zhong L, et al. Common activation mechanism of class A GPCRs. *Elife* 2019;8:e50279. <https://doi.org/10.7554/eLife.50279>.
- Weis W.I, Kobilka B.K. The molecular basis of G protein-coupled receptor activation. *Annu Rev Biochem* 2018;87:897–919. <https://doi.org/10.1146/annurev-biochem-060614-033910>.
- Rasmussen S.G, Choi H.J, Fung J.J, Pardon E, Casarosa P, Chae P.S, et al. Structure of a nanobody-stabilized active state of the beta(2) adrenoceptor. *Nature* 2011;469:175–80. <https://doi.org/10.1038/nature09648> .
- Rasmussen S.G, DeVree B.T, Zou Y, Kruse A.C, Chung K.Y, Kobilka T.S, et al. Crystal structure of the beta2 adrenergic receptor-Gs protein complex. *Nature* 2011;477:549–55. <https://doi.org/10.1038/nature10361>.
- Lamichhane R, Liu J.J, White K.L, Katritch V, Stevens R.C, Wüthrich K, et al. Biased Signaling of the G-Protein-Coupled Receptor β 2AR Is Governed by Conformational Exchange Kinetics. *Structure* 2020;28:371–377.e3. <https://doi.org/10.1016/j.str.2020.01.001>.
- Louet M, Casiraghi M, Damian M, Costa M.G, Renault P, Gomes A.A, et al. Concerted conformational dynamics and water movements in the ghrelin G protein-coupled receptor. *Elife* 2021;10:e63201. <https://doi.org/10.7554/elife.63201>.
- Rahmeh R, Damian M, Cottet M, Orcel H, Mendre C, Durroux T, et al. Structural insights into biased G protein-coupled receptor signaling revealed by fluorescence spectroscopy. *Proc Natl Acad Sci USA* 2012;109:6733–8. <https://doi.org/10.1073/pnas.1201093109> .
- Cong X, Maurel D, Déméné H.H, Vasiliauskaitė-brooks I, Hagelberger J, Peysson F, et al. Molecular insights into the μ -opioid receptor selective signaling. *Mol Cell* 2021;81:4165–75. <https://doi.org/10.1016/j.molcel.2021.07.033> .
- Okude J, Ueda T, Kofuku Y, Sato M, Nobuyama N, Kondo K, et al. Identification of a conformational equilibrium that determines the efficacy and functional selectivity of the mu-opioid receptor. *Angew Chem Int Ed Engl* 2015;54:15771–6. <https://doi.org/10.1002/ange.201508794>.
- Xu J, Hu Y, Kaindl J, Risel P, Hübner H, Maeda S, et al. Conformational complexity and dynamics in a muscarinic receptor revealed by NMR spectroscopy. *Mol Cell* 2019;75:53–65.e7. <https://doi.org/10.1016/j.molcel.2019.04.028>.
- M. Casiraghi, M. Damian, E. Lescop, E. Point, K. Moncoq, N. Morellet, et al., Functional Modulation of a G Protein-Coupled Receptor Conformational Landscape in a Lipid Bilayer, (2016). doi:10.1021/jacs.6b04432. .
- Liu J.J, Horst R, Katritch V, Stevens R.C, Wüthrich K. Biased signaling pathways in β 2-adrenergic receptor characterized by 19 F NMR. *Sci* (80-) 2012;335:1106–10. <https://doi.org/10.1126/science.1215802> .
- Suomivuori C.M, Latorraca N.R, Wingler L.M, Eismann S, King M.C, Kleinhenz A.L.W, et al. Molecular mechanism of biased signaling in a prototypical G protein-coupled receptor. *Science* 2020;367:881–7. <https://doi.org/10.1126/science.aaz0326> .
- Xu Z, Ikuta T, Kawakami K, Kise R, Qian Y, Xia R, et al. Structural basis of sphingosine-1-phosphate receptor 1 activation and biased agonism. *Nat Chem Biol* 2022;18:281–8. <https://doi.org/10.1038/s41589-021-00930-3>.
- Zheng K, Smith J.S, Eiger D.S, Warman A, Choi I, Honeycutt C.C, et al. Biased agonists of the chemokine receptor CXCR3 differentially signal through $G\alpha$ i: β -arrestin complexes. *Sci Signal* 2022;15:eabg5203. <https://doi.org/10.1126/scisignal.abg5203> .
- Bumbak F, Pons M, Inoue A, Paniagua J.C, Yan F, Wu H, et al. Ligands selectively tune the local and global motions of neurotensin receptor 1 (NTS1). *Cell Rep* 2023; 42:112015. <https://doi.org/10.1016/j.celrep.2023.112015> .
- Ferré G, Anazia K, Silva L.O, Thakur N, Ray A.P, Eddy M.T. Global insights into the fine tuning of human A2AAR conformational dynamics in a ternary complex with an engineered G protein viewed by NMR. *Cell Rep* 2022;41. <https://doi.org/10.1016/j.celrep.2022.111844>.
- Robben J.H, Knoers N.V.A.M, Deen P.M.T. Regulation of the vasopressin V2 receptor by vasopressin in polarized renal collecting duct cells. *Mol Biol Cell* 2004; 15:5693–9. <https://doi.org/10.1091/mbc.e04-04-0337>.
- Ren X, Reiter E, Ahn S, Kim J, Chen W, Lefkowitz R.J. Different G protein-coupled receptor kinases govern G protein and β -arrestin-mediated signaling of V2 vasopressin receptor. *Proc Natl Acad Sci USA* 2005;102:1448–53. <https://doi.org/10.1073/pnas.0409534102> .
- Alonso G, Galibert E, Boulay V, Guillou A, Jean A, Compan V, et al. Sustained elevated levels of circulating vasopressin selectively stimulate the proliferation of kidney tubular cells via the activation of V2 receptors. *Endocrinology* 2009;150: 239–50. <https://doi.org/10.1210/en.2008-0068> .
- Ball S.G. Vasopressin and disorders of water balance: the physiology and pathophysiology of vasopressin. *Ann Clin Biochem* 2007;44:417–31. <https://doi.org/10.1258/000456307781646030>.
- Morello J.P, Bichet D.G. Nephrogenic diabetes insipidus. *Annu Rev Physiol* 2001; 63:607–30. <https://doi.org/10.1146/annurev.physiol.63.1.607>.
- Bockenbauer D, Bichet D.G. Pathophysiology, diagnosis and management of nephrogenic diabetes insipidus. *Nat Rev Nephrol* 2015;11:576–88. <https://doi.org/10.1038/nrneph.2015.89>.
- Mouillac B, Mendre C. Pharmacological chaperones as potential therapeutic strategies for misfolded mutant vasopressin receptors. In: Ulloa-Avuirre A, Ya-Juung T, editors. *Target. Traffick. Drug Dev.* Springer; 2018. p. 63–83. https://doi.org/10.1007/164_2017_50.
- Jean-Alphonse F, Perkovska S, Frantz M.-C.C, Durroux T, Mejean C, Morin D, et al. Biased agonist pharmacochaperones of the AMP V2 receptor may treat congenital nephrogenic diabetes insipidus. *J Am Soc Nephrol* 2009;20:2190–203.

- <https://doi.org/10.1681/asn.2008121289>.
- [31] Rosenthal S.S, Feldman B.J, Vargas G.A, Gitelman S.E. Nephrogenic syndrome of inappropriate antidiuresis (NSIAD): a paradigm for activating mutations causing endocrine dysfunction. *Pediatr Endocrinol Rv* 2006;4:66–70. <https://doi.org/10.1056/nejmoa042743>.
- [32] Ballesteros J.A, Weinstein H. Integrated methods for the construction of three-dimensional models and computational probing of structure-function relations in G protein-coupled receptors. *Methods Neurosci* 1995;25:366–428. [https://doi.org/10.1016/S1043-9471\(05\)80049-7](https://doi.org/10.1016/S1043-9471(05)80049-7).
- [33] Erdélyi L.S, Mann W.A, Morris-Rosendahl D.J, Groß U, Nagel M, Várai P, et al. Mutation in the V2 vasopressin receptor gene, AVPR2, causes nephrogenic syndrome of inappropriate diuresis. *Kidney Int* 2015;88:1070–8. <https://doi.org/10.1038/ki.2015.181>.
- [34] Tiulpakov A, White C.W, Abhayawardana R.S, See H.B, Chan A.S, Seeber R.M, et al. Mutations of vasopressin receptor 2 including novel L312S have differential effects on trafficking. *Mol Endocrinol* 2016;30:889–904. <https://doi.org/10.1210/me.2016-1002>.
- [35] Vezzi V, Ambrosio C, Grò M.C, Molinari P, Stüral G, Costa T, et al. Vasopressin receptor 2 mutations in the nephrogenic syndrome of inappropriate antidiuresis show different mechanisms of constitutive activation for G protein coupled receptors. *Sci Rep* 2020;10:9111. <https://doi.org/10.1038/s41598-020-65996-w>.
- [36] Bous J, Orcel H, Floquet N, Leyrat C, Lai-Kee-Him J, Gaibelet G, et al. Cryo-electron microscopy structure of the antidiuretic hormone arginine-vasopressin V2 receptor signaling complex. *Sci Adv* 2021;7:eabg5628. <https://doi.org/10.1126/sciadv.abg5628>.
- [37] Zhou F, Ye C, Ma X, Yin W, Croll T.I, Zhou Q, et al. Molecular basis of ligand recognition and activation of human V2 vasopressin receptor. *Cell Res* 2021;31:929–31. <https://doi.org/10.1038/s41422-021-00480-2>.
- [38] Wang L, Xu J, Cao S, Sun D, Liu H, Lu Q, et al. Cryo-EM structure of the AVP-vasopressin receptor 2-Gs signaling complex. *Cell Res* 2021;31:932–4. <https://doi.org/10.1038/s41422-021-00483-z>.
- [39] Bous J, Fouillen A, Orcel H, Trapani S, Cong X, Fontanel S, et al. Structure of the vasopressin hormone-V2 receptor- β -arrestin1 ternary complex. *eab07761*. *Sci Adv* 2022;8. <https://doi.org/10.1101/2022.02.11.480047>.
- [40] Cong X, Fiorucci S, Golebiowski J. Activation dynamics of the neurotensin G protein-coupled receptor 1. *J Chem Theory Comput* 2018;14:4467–73. <https://doi.org/10.1021/acs.jctc.8b00216>.
- [41] Cong X, Chéron J.B, Golebiowski J, Antonczak S, Fiorucci S. Allosteric modulation mechanism of the mGluR5 transmembrane domain. *J Chem Inf Model* 2019;59:2871–8. <https://doi.org/10.1021/acs.jcim.9b00045>.
- [42] Erlanson S.C, Rawson S, Osei-Owusu J, Brock K.P, Liu X, Paulo J.A, et al. The relaxin receptor RXFP1 signals through a mechanism of autoinhibition. *Nat Chem Biol* 2023;19:1013–21. <https://doi.org/10.1038/s41589-023-01321-6>.
- [43] Webb B, Sali A. Comparative protein structure modeling using modeller. 5.6.1-5.6.37. *Curr Protoc Bioinforma* 2016;54. <https://doi.org/10.1002/cpbi.3>.
- [44] Waltenspihl Y, Schöppe J, Ehrenmann J, Kummer L, Plückthun A. Crystal structure of the human oxytocin receptor. *Sci Adv* 2020;6:1–12. <https://doi.org/10.1126/sciadv.abb5419>.
- [45] Eberhardt J, Santos-Martins D, Tillack A.F, Forli S. AutoDock Vina 1.2.0: new docking methods, expanded force field, and python bindings. *J Chem Inf Model* 2021;61:3891–8. <https://doi.org/10.1021/acs.jcim.1c00203>.
- [46] Schott-Verdugo S, Gohlke H. PACKMOL-memgen: a simple-to-use, generalized workflow for membrane-protein-lipid-bilayer system building. *J Chem Inf Model* 2019;59. <https://doi.org/10.1021/acs.jcim.9b00269>.
- [47] Lindorff-Larsen K, Piana S, Palmo K, Maragakis P, Klepeis J.L, Dror R.O, et al. Improved side-chain torsion potentials for the Amber ff99SB protein force field. *Proteins* 2010;78:1950–8. <https://doi.org/10.1002/prot.22711>.
- [48] Wang J, Wolf R.M, Caldwell J.W, Kollman P.A, Case D.A. Development and testing of a general amber force field. *J Comput Chem* 2004;25:1157–74. <https://doi.org/10.1002/jcc.20035>.
- [49] Dickson C.J, Madej B.D, Skjervek Å.A, Betz R.M, Teigen K, Gould I.R, et al. Lipid14: the amber lipid force field. *J Chem Theory Comput* 2014;10:865–79. <https://doi.org/10.1021/ct4010307>.
- [50] Jorgensen W.L, Chandrasekhar J, Madura J.D, Impey R.W, Klein M.L. Comparison of simple potential functions for simulating liquid water. *J Chem Phys* 1998;79:926. <https://doi.org/10.1063/1.445869>.
- [51] Joung I.S, Cheatham T.E. Determination of alkali and halide monovalent ion parameters for use in explicitly solvated biomolecular simulations. *J Phys Chem B* 2008;112:9020–41. <https://doi.org/10.1021/jp8001614>.
- [52] Wang J, Cieplak P, Kollman P. How well does a restrained electrostatic potential (RESP) model perform in calculating conformational energies of organic and biological molecules? *J Comput Chem* 2000;21:1011–117.
- [53] Van Der Spoel D, Lindahl E, Hess B, Groenhof G, Mark A.E, Berendsen H.J.C. GROMACS: fast, flexible, and free. *J Comput Chem* 2005;26:1701–18. <https://doi.org/10.1002/jcc.20291>.
- [54] Tribello G, Bonomi M, Branduardi D, Bussi C. PLUMED 2: new feathers for an old bird. *Comput Phys Commun* 2014;185:604–13. <https://doi.org/10.1016/j.cpc.2013.09.018>.
- [55] Wang L, Friesner R.A, Berne B.J. Replica exchange with solute scaling: a more efficient version of replica exchange with solute tempering (REST2). *J Phys Chem B* 2011;115:9431–8. <https://doi.org/10.1021/jp204407d>.
- [56] Patriksson A, Van Der Spoel D. A temperature predictor for parallel tempering simulations. *Phys Chem Chem Phys* 2008;10:2073–7. <https://doi.org/10.1039/b716554d>.
- [57] Morello J.P, Bouvier M, Petäjä-Repo U.E, Bichet D.G. Pharmacological chaperones: a new twist on receptor folding. *Trends Pharmacol Sci* 2000;21:466–9. [https://doi.org/10.1016/s0165-6147\(00\)01575-3](https://doi.org/10.1016/s0165-6147(00)01575-3).
- [58] Bokoch M.P, Zou Y, Rasmussen S.G.F, Liu C.W, Nygaard R, Rosenbaum D.M, et al. Ligand-specific regulation of the extracellular surface of a G-protein-coupled receptor. *Nature* 2010;463:108–12. <https://doi.org/10.1038/nature08650>.
- [59] Soumier R, Mas C, Steyaert J, Laeremans T, Manglik A, Huang W, et al. Propagation of conformational changes during μ -opioid receptor activation. *Nature* 2015;524:375–8. <https://doi.org/10.1038/nature14680>.
- [60] Cox J, Mann M. MaxQuant enables high peptide identification rates, individualized p.p.b.-range mass accuracies and proteome-wide protein quantification. *Nat Biotechnol* 2008;26:1367–72. <https://doi.org/10.1038/nbt.1511>.
- [61] Frantz M.C, Pellissier L.P, Pflimlin E, Loison S, Gandia J, Marsol C, et al. LIT-001, the first nonpeptide oxytocin receptor agonist that improves social interaction in a mouse model of autism (doi:doi/). *J Med Chem* 2018;61:8670–92. <https://doi.org/10.1021/acs.jmedchem.8b00>.
- [62] Delaglio F, Grzesiek S, Vuister G.W, Zhu G, Pfeifer J, Bax A. NMRPipe: a multidimensional spectral processing system based on UNIX pipes. *J Biomol NMR* 1995 63 1995;6:277–93. <https://doi.org/10.1007/BF00197809>.
- [63] Johnson B.A, Blevins R.A. NMR view: a computer program for the visualization and analysis of NMR data. *J Biomol NMR* 1994 45 1994;4:603–14. <https://doi.org/10.1007/BF00404272>.
- [64] Loison S, Cottet M, Orcel H, Adihou H, Rahmeh R, Lamarque L, et al. Selective fluorescent nonpeptidic antagonists for vasopressin V₂ GPCR: application to ligand screening and oligomerization assays. *J Med Chem* 2012;55:8588–602. <https://doi.org/10.1021/jm3006146>.
- [65] Zwier J.M, Roux T, Cottet M, Durroux T, Douzon S, Bdioui S, et al. A fluorescent ligand-binding alternative using Tag-lite® technology. *J Biomol Screen* 2010;15:1248–59. <https://doi.org/10.1177/1087057110384611>.
- [66] Tenenbaum J, Ayoub M.A, Perkovska S, Adra-Delenne A.L, Mendre C, Ranchin B, et al. The constitutively active V2 receptor mutants conferring NSIAD are weakly sensitive to agonist and antagonist regulation. *PLoS One* 2009;4:e8383. <https://doi.org/10.1371/journal.pone.0008383>.
- [67] Namkung Y, Le Guillou C, Lukashova V, Kobayashi H, Hogue M, Khoury E, et al. Monitoring G protein-coupled receptor and β -arrestin trafficking in live cells using enhanced bystander BRET. *Nat Commun* 2016;7. <https://doi.org/10.1038/ncomms12178>.
- [68] Quoyer J, Janz J.M, Luo J, Ren Y, Armando S, Lukashova V, et al. Pepducin targeting the C-X-C chemokine receptor type 4 acts as a biased agonist favoring activation of the inhibitory G protein. *Proc Natl Acad Sci* 2013;110:E5088–97. <https://doi.org/10.1073/pnas.1312515110>.
- [69] Kimbrough R.D.J, Cash W.D, Branda L.A, Chan W, Du Vigneau V. Synthesis and biological properties of 1-desamino-8-lysine-vasopressin. *J Biol Chem* 1963;238:1411–4. [https://doi.org/10.1016/S0021-9258\(18\)81197-8](https://doi.org/10.1016/S0021-9258(18)81197-8).
- [70] Tabata H, Yoneda T, Oshitari T, Takahashi H, Natsugari H. Tolvaptan-type vasopressin receptor ligands: important role of axial chirality in the active form. *J Med Chem* 2017;60:4503–9. <https://doi.org/10.1021/acs.jmedchem.7bB00422>.
- [71] Liu H.L, Zhong H.Y, Zhang Y.X, Xue H.R, Zhang Z.S, Fu K.Q, et al. Structural basis of tolvaptan binding to the vasopressin V2 receptor. *Acta Pharmacol Sin* 2024;45:2441–9. <https://doi.org/10.1038/S41401-024-01325-5>.
- [72] Nygaard R, Zou Y, Dror R.O, Mildorf T.J, Arlow D.H, Manglik A, et al. The dynamic process of beta(2)-adrenergic receptor activation. *Cell* 2013;152:532–42. <https://doi.org/10.1016/j.cell.2013.01.008>.
- [73] Ye L, Van Eps N, Zimmer M. P. Oliver, receptor by conformational selection. *Nature* 2016;533:265–8. <https://doi.org/10.1038/nature17668>.
- [74] Zhao J, Elgeti M, O'Brien E.S, Sár C.P, El Daibani A, Heng J, et al. Ligand efficacy modulates conformational dynamics of the μ -opioid receptor. *Nature* 2024;629. <https://doi.org/10.1038/s41586-024-07295-2>.
- [75] El Daibani A, Paggi J.M, Kim K, Laloudakis Y.D, Popov P, Bernhard S.M, et al. Molecular mechanism of biased signaling at the kappa opioid receptor. *Nat Commun* 2023;14:1338. <https://doi.org/10.1038/s41467-023-37041-7>.
- [76] Lee H.J, Lee H.S, Youn T, Byrne B, Chae P.S. Impact of novel detergents on membrane protein studies. *Chem* 2022;8:980–1013. <https://doi.org/10.1016/j.chempr.2022.02.007>.
- [77] Thakur N, Ray A.P, Jin B, Afsharian N.P, Lyman E, Gao Z.G, et al. Membrane mimetic-dependence of GPCR energy landscapes. *Structure* 2024. <https://doi.org/10.1016/j.str.2024.01.013>.
- [78] Zhang Y, Sun B, Feng D, Hu H, Chu M, Qu Q, et al. Cryo-EM structure of the activated GLP-1 receptor in complex with a G protein. *Nat Publ Gr* 2017;546:248–53. <https://doi.org/10.1038/nature22394>.
- [79] Liang Y.-L, Khoshouei M, Radjainia M, Zhang Y, Glukhova A, Tarrasch J, et al. Phase-plate cryo-EM structure of a class B GPCR-G-protein complex. *Nature* 2017;546:118–23. <https://doi.org/10.1038/nature22327>.
- [80] Iwahara J, Tang C, Marius Clore G. Practical aspects of (1)H transverse paramagnetic relaxation enhancement measurements on macromolecules. *J Magn Reson* 2007;184:185–95. <https://doi.org/10.1016/j.jmr.2006.10.003>.
- [81] Mirzadegan T, Benko G, Filipek S, Palczewski K. Sequence analyses of G-protein-coupled receptors: similarities to rhodopsin. *Biochemistry* 2003;42:2759–67. <https://doi.org/10.1021/bi027224>.
- [82] Kosugi S, Hai N, Okamoto H, Sugawa H, Mori T. A novel activating mutation in the thyrotropin receptor gene in an autonomously functioning thyroid nodule developed by a Japanese patient. *Eur J Endocrinol* 2000;143:471–7. <https://doi.org/10.1530/eje.0.1430471>.
- [83] Ceraudo E, Horioka M, Mattheisen J.M, Hitchman T.D, Moore A.R, Kazmi M.A, et al. Direct evidence that the GPCR CysLTR2 mutant causative of uveal melanoma is constitutively active with highly biased signaling. *J Biol Chem* 2021;296:100163. <https://doi.org/10.1074/jbc.RA120.015352>.

- [84] Mo X.L, Yang R, Tao Y.X. Functions of transmembrane domain 3 of human melanocortin-4 receptor. *Mol Endocrinol* 2012;49:221–35. <https://doi.org/10.1530/jme-12-0162>
- [85] Chen Q, Tesmer J.J.G. G protein-coupled receptor interactions with arrestins and GPCR kinases: The unresolved issue of signal bias. *J Biol Chem* 2022;298. <https://doi.org/10.1016/j.jbc.2022.102279>
- [86] Duan J, Liu H, Zhao F, Yuan Q, Ji Y, Cai X, et al. GPCR activation and GRK2 assembly by a biased intracellular agonist. *Nature* 2023;620:676–81. <https://doi.org/10.1038/s41586-023-06395-9>
- [87] Chen Q, Plasencia M, Li Z, Mukherjee S, Patra D, Chen C.L, et al. Structures of rhodopsin in complex with G-protein-coupled receptor type 1. *Nature* 2021;595:600–5. <https://doi.org/10.1038/s41586-021-03721-x>
- [88] McCorvy J.D, Wacker D, Wang S, Agegnehu B, Liu J, Lansu K, et al. Structural determinants of 5-HT_{2B} receptor activation and biased agonism. *Nat Struct Mol Biol* 2018;25:787–96. <https://doi.org/10.1038/s41594-018-0116-7>
- [89] Cao D, Yu J, Wang H, Luo Z, Liu X, He L, et al. Structure-based discovery of nonhallucinogenic psychedelic analogs. *Science* 2022;375:403–11. <https://doi.org/10.1126/scienceE.abl8615>
- [90] Xu Z, Ikuta T, Kawakami K, Kise R, Qian Y, Xia R, et al. Structural basis of sphingosine-1-phosphate receptor 1 activation and biased agonism. *Nat Chem Biol* 2022;18:281–8. <https://doi.org/10.1038/s41589-021-00930-3>
- [91] Nivedha A.K, Lee S, Vaidehi N. Biased agonists differentially modulate the receptor conformation ensembles in Angiotensin II type 1 receptor. *J Mol Graph Model* 2023;118:108365. <https://doi.org/10.1016/j.jmgm.2022.108365>
- [92] Wang H, Hetzer F, Huang W, Qu Q, Meyerowitz J, Kaindl J, et al. Structure-based evolution of G protein-biased -opioid receptor agonists. *Angew Chem Int Ed* 2022;61:e202200269.
- [93] Schönege A.M, Gallion J, Picard L.P, Wilkins A.D, Le Gouill C, Audet M, et al. Evolutionary action and structural basis of the allosteric switch controlling functional selectivity. *Commun* 2017;8:2169. <https://doi.org/10.1038/s41467-017-02257-x>
- [94] Wingler L.M, Skiba M.A, McMahon C, Staus D.P, Kleinhenz A.L.W, Suomivuori C.M, et al. Angiotensin and biased analogs induce structurally distinct active conformations within a GPCR. *Sci (80-)* 2020;367:888–92. <https://doi.org/10.1126/science.aay9813>

Biased activation of the vasopressin V2 receptor probed by molecular dynamics simulations, NMR and pharmacological studies.

Aurélien Fouillen^{a,1}, Pierre Couvineau^{a,1}, Gérald Gaibelet^{a,1}, Stéphanie Riché^b, Hélène Orcel^a, Christiane Mendre^a, Ali Kanso^a, Romain Lanotte^a, Julie Nguyen^a, Juliette Dimon^a, Serge Urbach^a, Rémy Sounier^a, Sébastien Granier^a, Dominique Bonnet^b, Xiaojing Cong^{*,a}, Bernard Mouillac^{*,a}, Hélène Déméné^{*,c,2}

^aInstitut de Génomique Fonctionnelle, Université de Montpellier, CNRS, INSERM, 34094 Montpellier cedex 5, France ; ^bLaboratoire d'Innovation Thérapeutique, UMR7200 CNRS, Université de Strasbourg, Institut du Médicament de Strasbourg, 67412 Illkirch-Graffenstaden, France ; ^cCentre de Biologie Structurale (CBS), Univ Montpellier, INSERM, CNRS, 34090, Montpellier, France

¹These authors contributed equally to this work

*Corresponding authors: Hélène Déméné (helene.demene@cbs.cnrs.fr), Bernard Mouillac (bernard.mouillac@igf.cnrs.fr) and Xiaojing Cong (xiaojing.cong@igf.cnrs.fr).

²Lead contact: Hélène Déméné, at Centre de Biologie Structurale, Université de Montpellier, INSERM, CNRS, 29, rue de Navacelles, 34090 Montpellier Cedex, France. Tel: +33 (0) 4 67 41 77 01
helene.demene@cbs.cnrs.fr

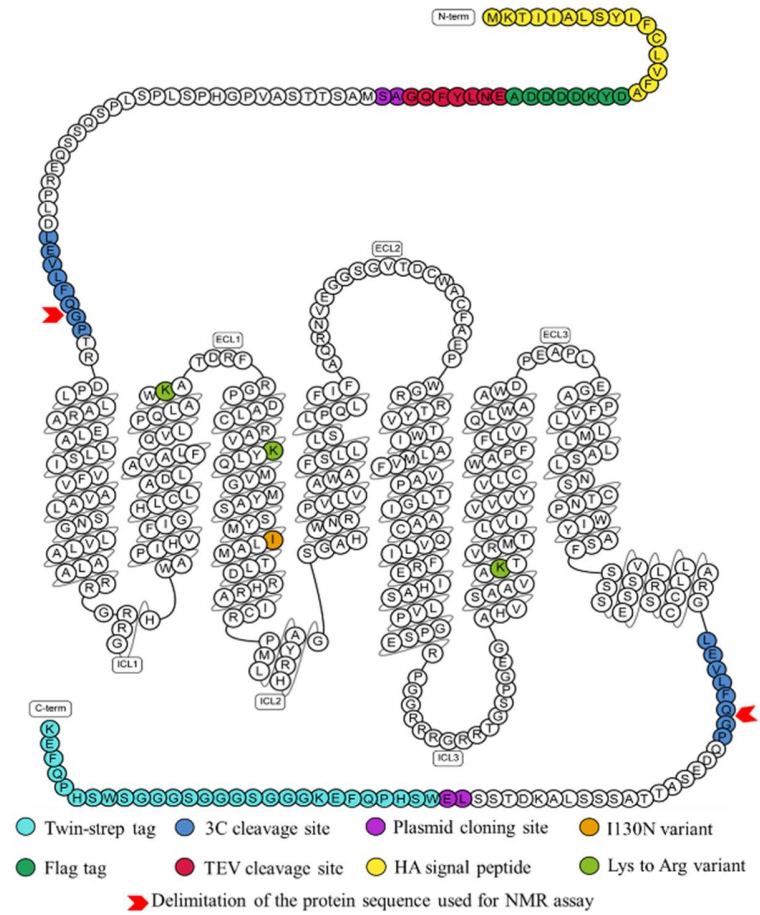
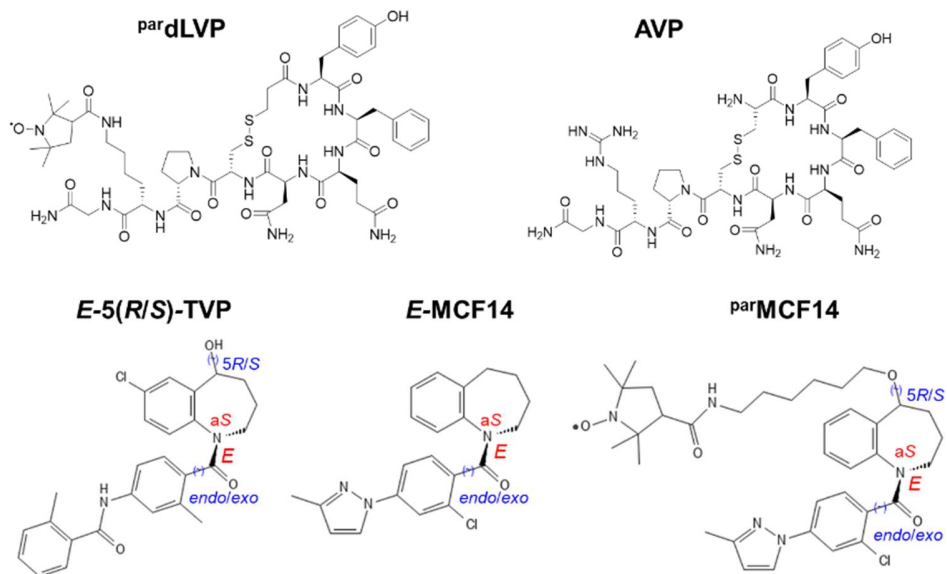
A**B**

Figure S1. Engineering of V2R and ligands (related to Figure 1). (A) Snake plot of the V2R sequence used in this study. The hemagglutinin (HA) signal peptide (MKTIIALSYIFCLVFA, in yellow) followed by a Flag-tag (DYKDDDDA, in dark green) and a TEV protease cleavage site (ENLYFQG, in red) were added at the N-terminus, while a Twin-strep-tag® (WSHPQFEKGGGSGGGSGGGSWHPQFEK, in cyan) was inserted at the C-terminus. In addition, N22 was substituted with a glutamine residue to avoid N-glycosylation, and C358 mutated into an alanine to eliminate potential intermolecular disulfide bridges during solubilization and purification. Two HRV3C protease cleavage sites (LEVLFQGP, in blue) were also added to remove the N- and C-termini and enhance the NMR spectra quality, one in the N-terminus between D30 and T31 and one in the C-terminus between G345 and Q354 (replacing R346-TPPSLG-P353). M1 and L2 residues were replaced by A and S residues (purple), and LE residues (purple) were added just before the Twin-strep-tag®, during subcloning (by introduction of a Nhe1 and a Xho1 restriction site, respectively). Mutation sites of K100^{2.65}R, K116^{3.29}R, and K268^{6.32}R are indicated in light green, and I130^{3.43}N in orange. The two red head-arrows indicate N- and C-termini of the V2R protein after HRV3C cleavage. (B) Chemical structures of the ligands (see Figure S3 for the synthesis). For TVP and MCF14, both *endo/exo* isomers were tested in MD simulations. The *endo*-isomer turned out to bind more stably. Therefore, only the *endo*-isomer of ^{par}MCF14 was used for MD simulations.

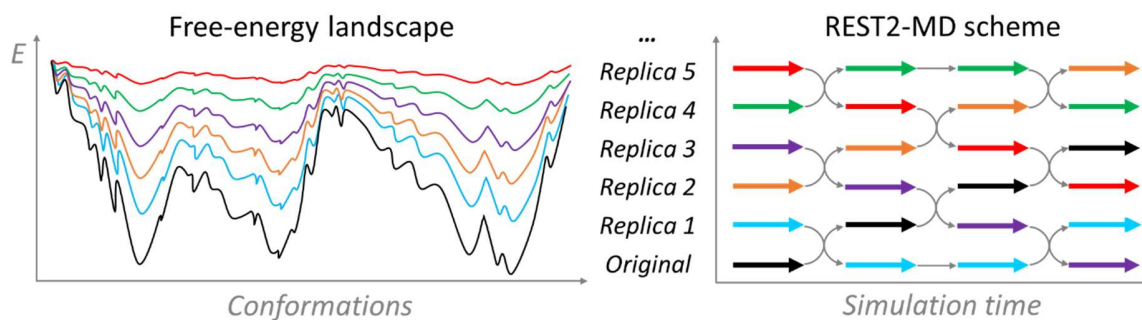


Figure S2. Scheme of REST2 protocol. REST2 is a type of Hamiltonian replica exchange simulation scheme, which performs many replicas of the same MD simulation system simultaneously. The replicas have modified free energy surfaces, in which the barriers are easier to cross than in the original system. By frequently swapping the conformations between neighbor replicas during the MD, the simulations “travel” on different free energy surfaces and easily visit different conformational zones. Finally, only the samples on the original free energy surface are collected. REST2, in particular, modifies the free energy surfaces by reducing the energy barriers of conformational changes of “solute” molecules in the simulation system. Here, the protein and the ligands were considered as “solute”, in order to facilitate their conformational changes.

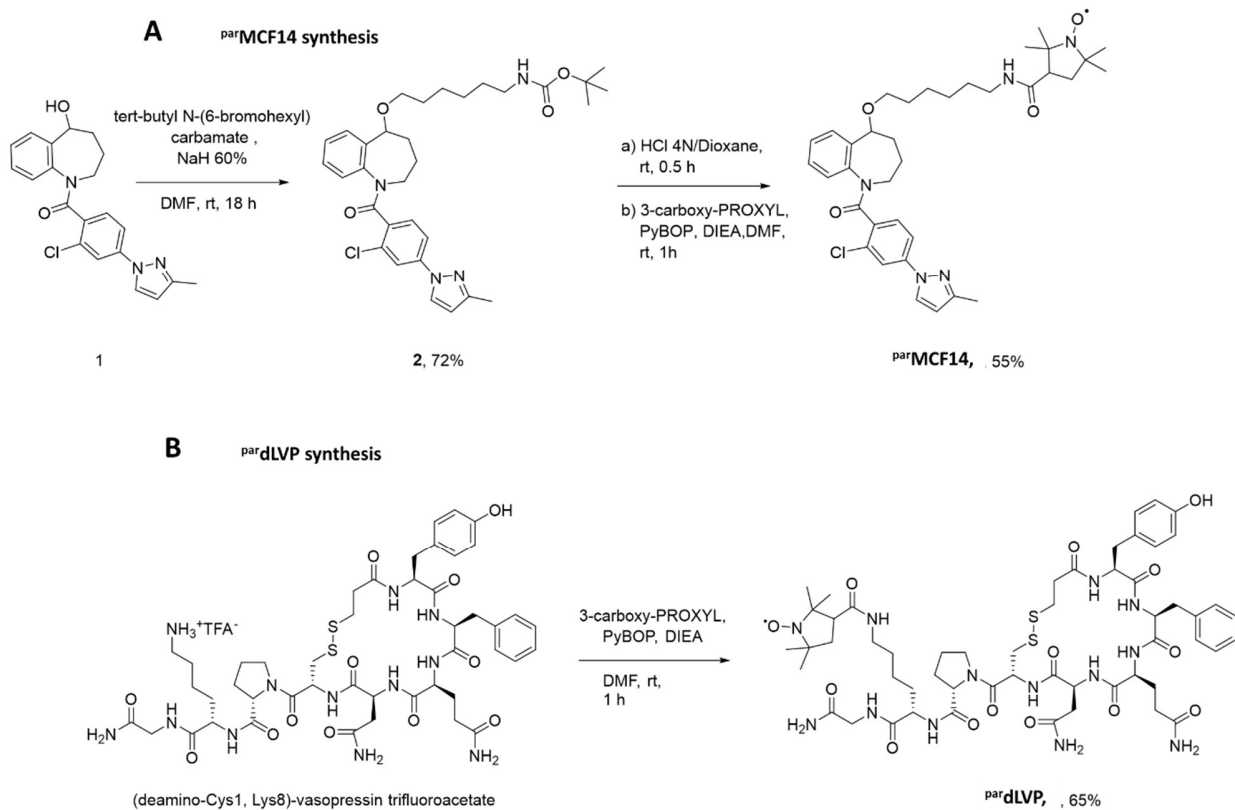


Figure S3. Synthesis of paramagnetic ligands: (A) ^{par}MCF14 and (B) ^{par}dLVP (related to Figure 1). The procedures are fully detailed in the Material and Methods section.

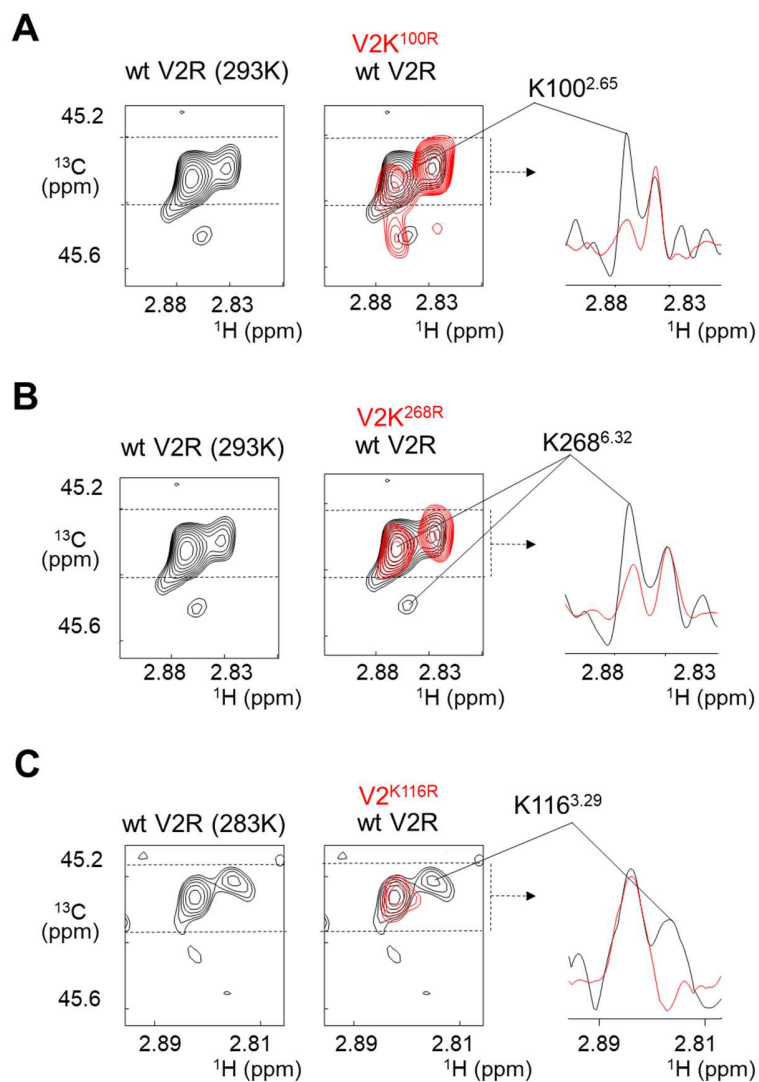
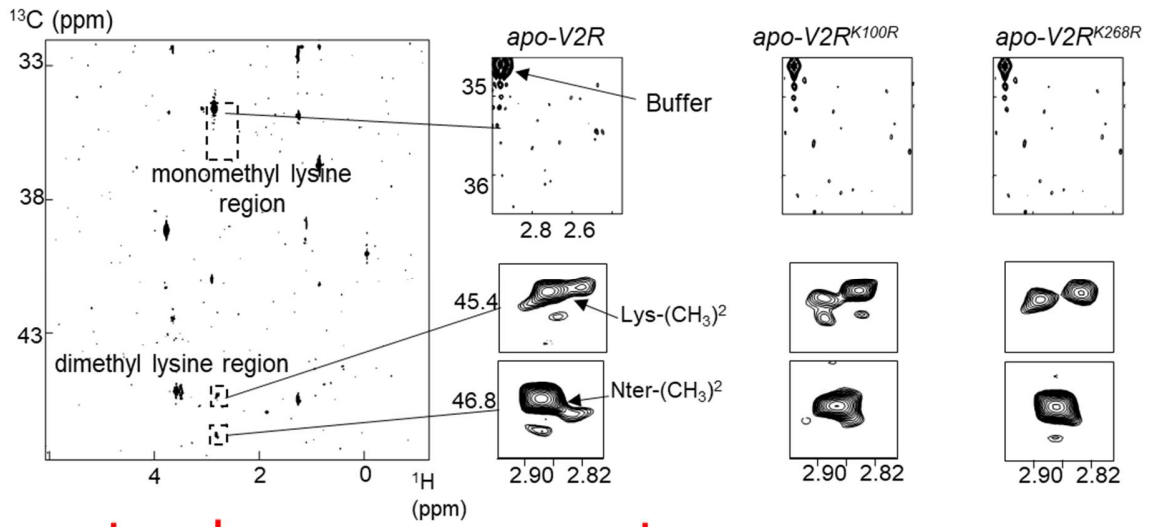
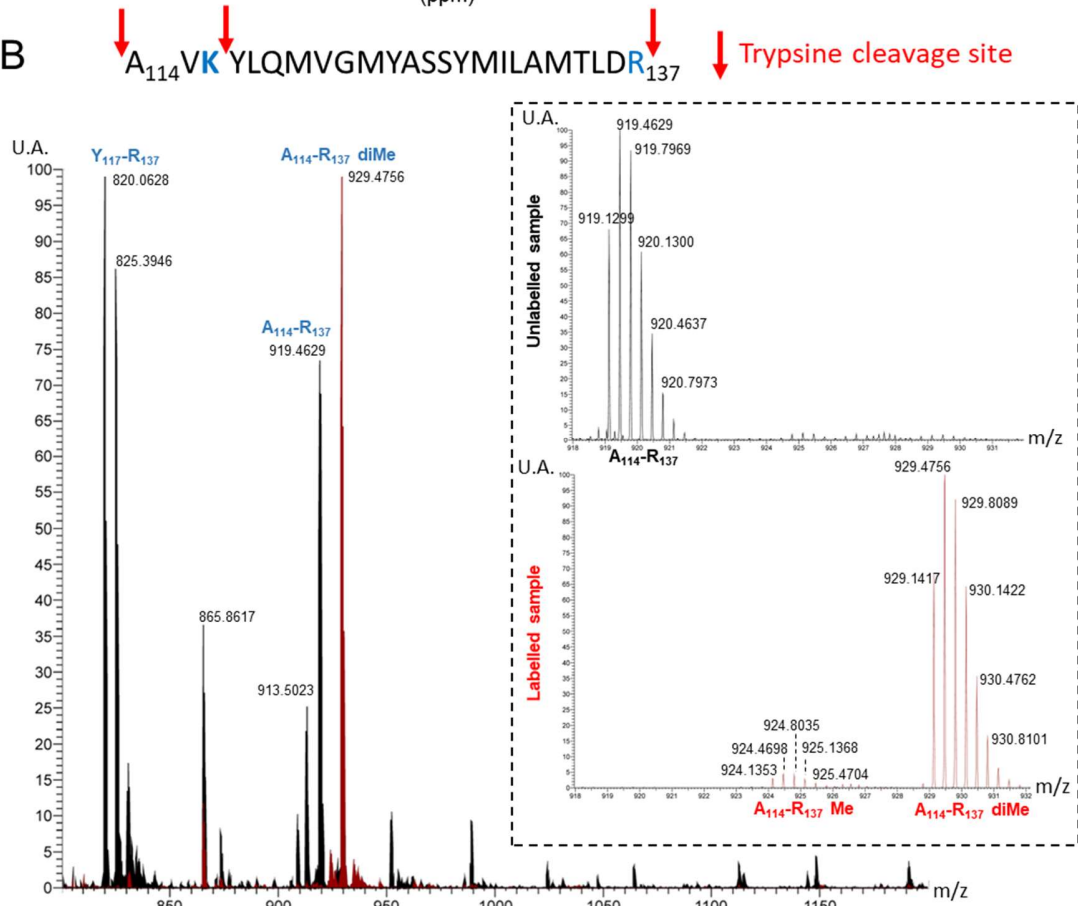


Figure S4. Assignment of correlation peaks of dimethylated lysines (related to Figure 1). Extracted HMQC spectrum of native V2R (black) is superimposed on that of the mutants (red): (A) K100^{2.65}R, (B) K268^{6.32}R and (C) K116^{3.29}R. Experiments were run at 293 K, except for the assignment of the K116 resonance (283 K). On the right panels, we highlight the peak disappearance for each mutant (red line) as compared to native V2R (black line) in the ^1H dimension. The 1D projections along the ^{13}C dimension of ^1H rows between the two dashed lines are indicated by an arrow (right panels).

A apo-V2R



B



C

	Sequence	Peak area (10e6)			Ratio (Unlabelled : Me : diMe) (%)
		Unlabelled	Labelled - Me	Labelled - diMe	
Unlabelled	A114 - R137	1,440	/	18	98.8 : 0 : 1.2
	Y117 - R137	3,785	/	/	100 : 0 : 0
Labelled	A114 - R137	1	63	1,476	0.1 : 4.1 : 95.8
	Y117 - R137	0	/	/	0 : 0 : 0

Figure S5. Analysis of lysine methylation by (A) NMR and (B-C) mass spectrometry (related to Figure 1). (A) Identification of the mono-lysine and dimethyl-lysine regions in a representative HMQC spectrum acquired from purified samples of WT and mutant apo-V2R. The black boxes and their corresponding close-up views indicate location of monomethyl and dimethyl regions. The zoom for the monomethyl region was centered on the theoretical region 2.4-3 ppm/34.5-36.5 ppm in the ^1H and ^{13}C dimension respectively. The signal seen in the monomethyl lysine region only arises from the Hepes buffer, no specific signal is detected for monomethylated lysines. In the dimethyl-lysine region, peaks arising from labeled lysines ($\text{Lys}-(\text{CH}_3)_2$) and the N-terminal of the V2R ($\text{Nter}-(\text{CH}_3)_2$), generated after HRV3C cleavage, are shown. (B) Comparison of unlabeled and ^{13}C -methylated V2R by mass spectrometry (Material and Methods section). The analysis has been performed on the $\text{V2R}^{\text{K100R}}$ mutant, displaying only 2 lysine residues after HRV3C cleavage (K116 and K268, see Figure S1A). For clarity, only the tryptic peptide containing K116 (A114-R137, with the trypsin cleavage sites shown by red arrows) is represented in the B panel. Equivalent results were obtained for the peptide encompassing K268 (R252-R271). Sum of MS spectra from 67.3 to 67.8 min (m/z limited to 800-1200) obtained from unlabeled and ^{13}C -methylated V2R are superimposed: unlabeled peptides are shown in black, whereas the ^{13}C -methylated peptides are depicted in red. Peaks arising from A114-R137 and Y117-R137 can be detected in the unlabeled sample. Only a major peak corresponding to ^{13}C -dimethylated lysine A114-R137 peptide is seen in the labeled sample. Close-up views are displayed on the right: in the unlabeled sample, only signal for A114-R137 is measured, whereas in the labeled sample, monomethylated A114-R137 (very low intensity) and dimethylated A114-R137 (high intensity) are measured. A m/z difference of 10 (919 versus 929) between unlabeled and dimethyl-labeled lysine is measured, which means a mass difference of 30 (the peptide contains 3 charges) corresponding to two methyl groups. In addition, a m/z difference of 5 (919 versus 924) between unlabeled and monomethyl-labeled lysine is measured, which means a mass difference of 15 (3 charges) corresponding to one methyl group. (C) Methylation ratio of the representative A114-R137 tryptic peptide of the $\text{V2R}^{\text{K100R}}$ mutant. Peak areas corresponding to the unlabeled, mono- and dimethyl-labeled lysine are calculated. In the unlabeled sample, A114-R137 and Y117-R137 peptides are detected: for both peptides, the unlabeled species are major (1,440 and 3,785 units, respectively), as compared to no signal (*l*) or very minor signal (18 units) for the dimethyl-labeled lysine in the A114-R137 peptide. In the labeled sample, the A114-R137 dimethyl-labeled lysine peptide is almost exclusive (1,476 units versus 1 for unlabeled and 63 for the monomethyl-labeled), and the Y117-R137 is not detected (a 0 value means <1). Therefore, it appears that reductive dimethylation of the V2R onto its lysine residues is nearly complete with more than 95% efficiency.

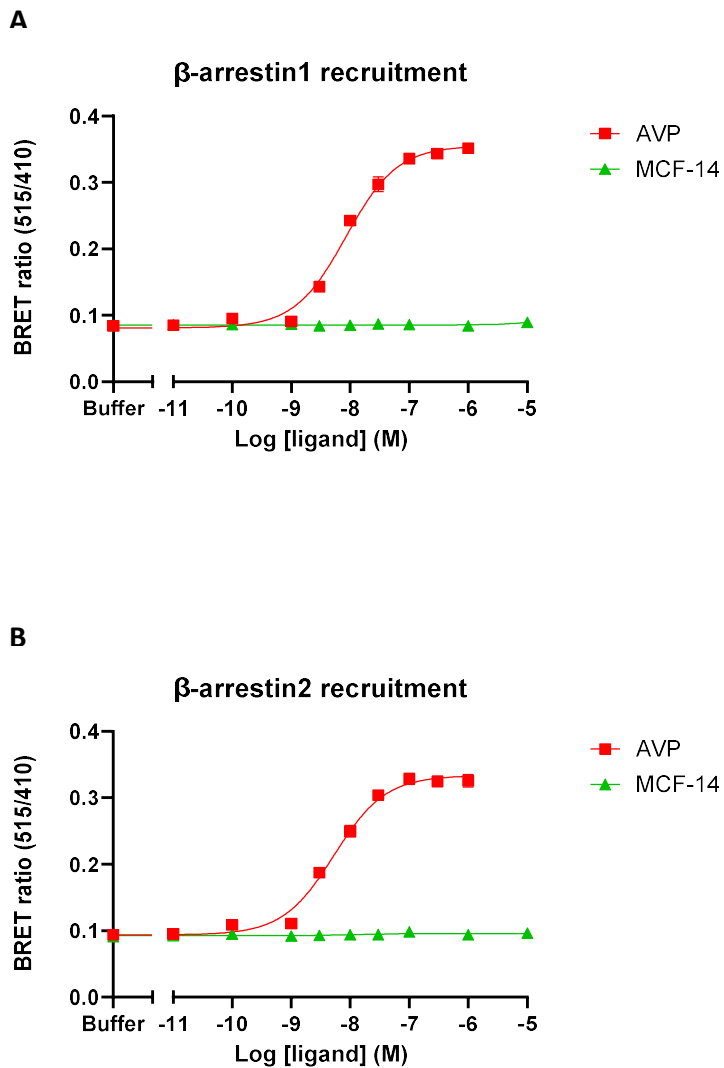
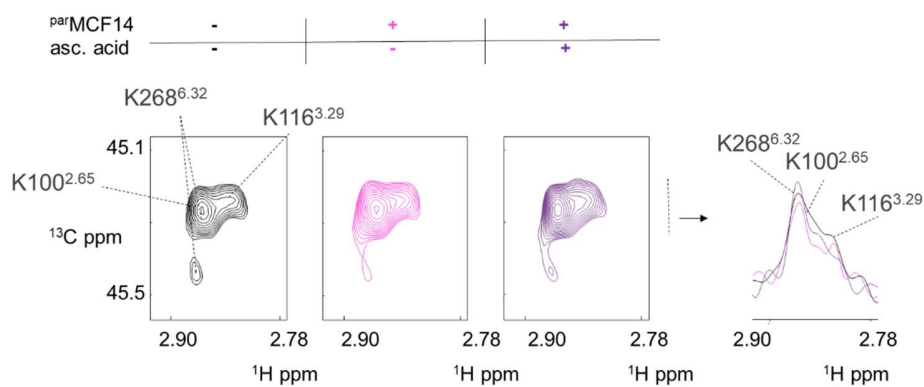


Figure S6. Inability of MCF14 to recruit β Arres (related to Figures 1 and 2). The V2R-dependent recruitment of (A) β Arr1 and (B) β Arr2 was evaluated upon increasing concentrations of AVP and MCF14 using BRET. As indicated in the Material and Methods, BRET was measured by energy transfer between β Arr-RlucII and membrane-anchored rGFP-CAAX (515 nm/ 410 nm ratio). The more β Arres are translocated to the membrane, the more the BRET signal. For each β Arr recruitment, a typical experiment is represented from at least 3 independent experiments, each point performed in triplicate. Each value is presented as mean \pm SEM.

A



B

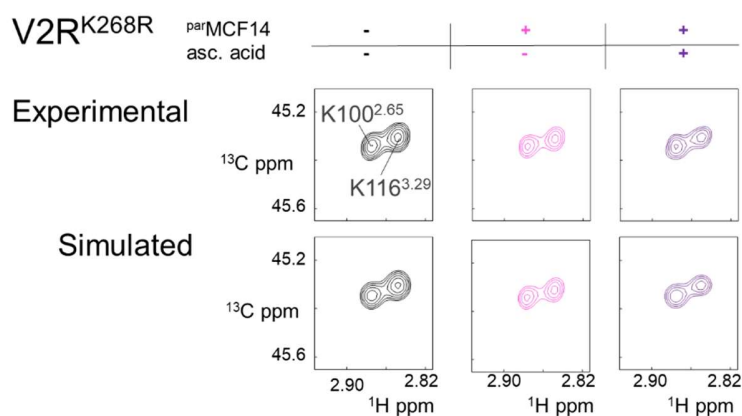


Figure S7. Effect of ^{par}MCF14 binding and reduction by ascorbic acid on the lysine HMQC correlation peaks of V2R and fitting procedure (related to Figure 2B). (A) The 1D projection along the ¹³C dimension of ¹H rows, is indicated by an arrow, showing a specific effect according to each lysine. (B) Experimental and simulated HMQC correlation of V2R^{K268R} in the apo-, ^{par}MCF- and ^{par}MCF14_{red}-bound states (recorded at 293K).

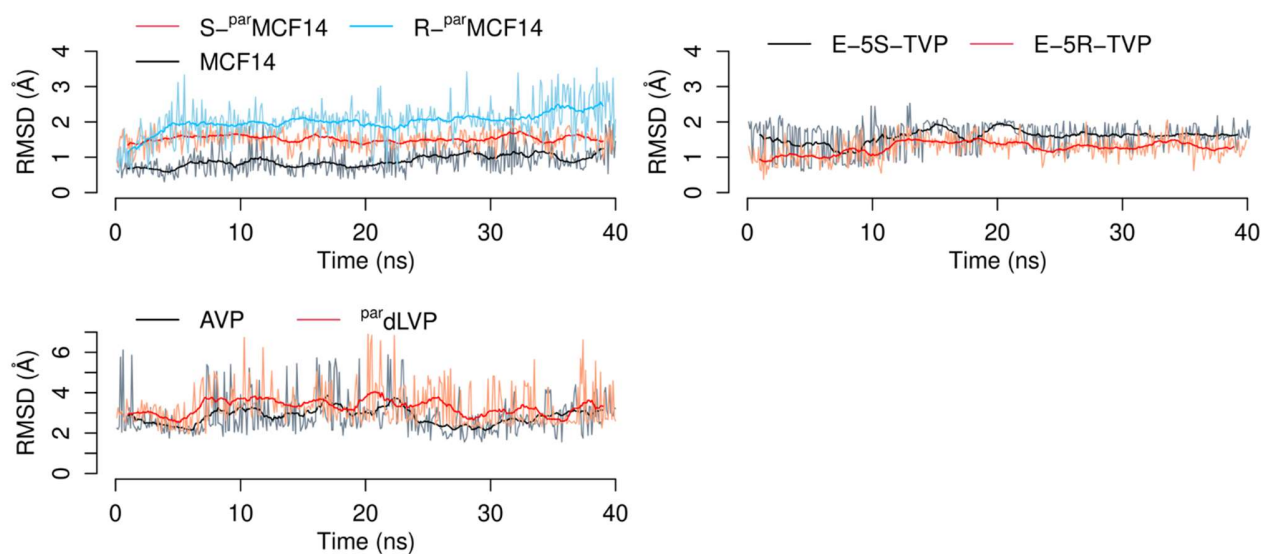


Figure S8. Conformational dynamics of V2R ligands during MD simulations (related to Figures 2 and 3). Ligand RMSD calculated for the non-hydrogen atoms of MCF14 and TVP, or the backbone atoms of AVP and ^{par}dLVP, excluding the paramagnetic tag.

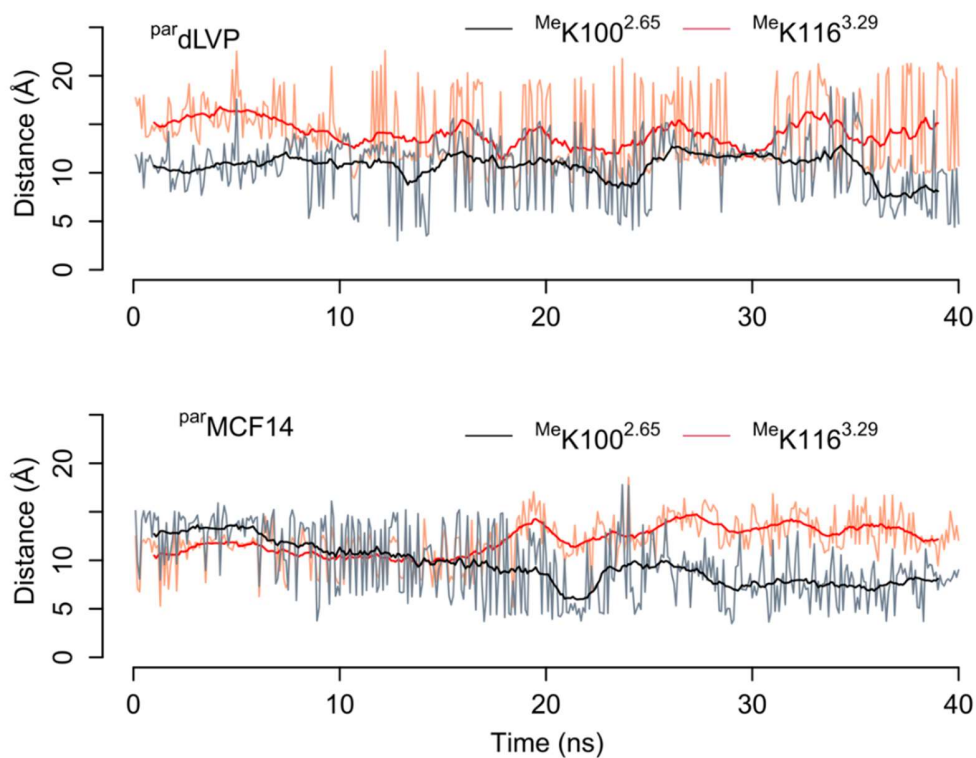


Figure S9. Distances between the paramagnetic tag and dimethylated K100^{2.65} and K116^{3.29} during two independent MD simulations (related to Figure 2D). The distance was measured between the nitroxide oxygen atom and nitrogen atom of the lysine side chain. In both ligands, the tag was (on average) closer to K100^{2.65} than K116^{3.29}. The equilibration phase was discarded

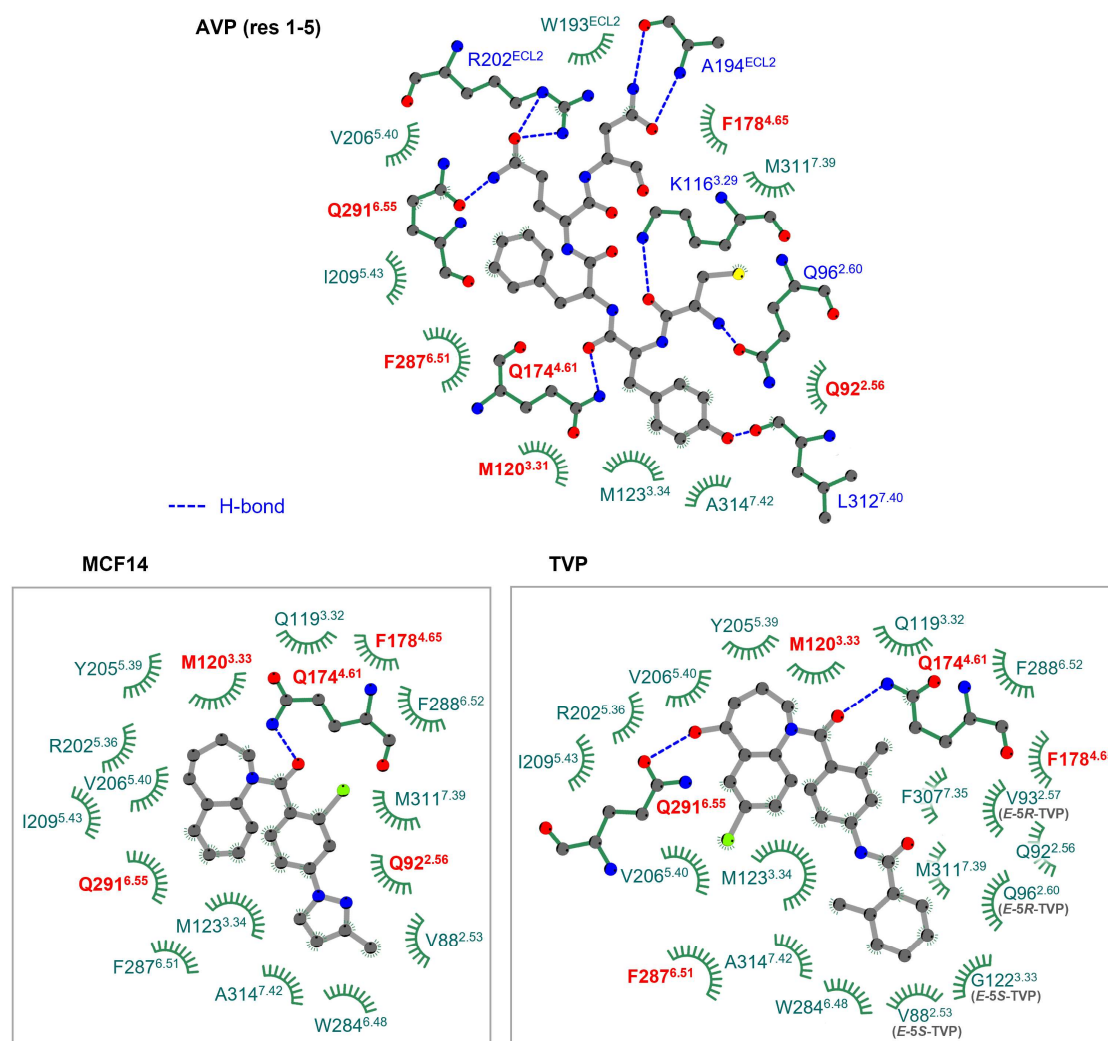


Figure S10. 2D interaction profile of the ligands with the V2R orthosteric pocket (related to Figure 3A). The detailed maps show H-bonds and hydrophobic contacts within 4 Å of AVP (residues 1-5), MCF14 and TVP. For TVP, different contacts between the two enantiomers are labeled, whereas the H-bonds are common for both enantiomers. Residues that significantly affected ligand binding affinity upon site-directed mutagenesis in this study (Figure 4) are highlighted in red.

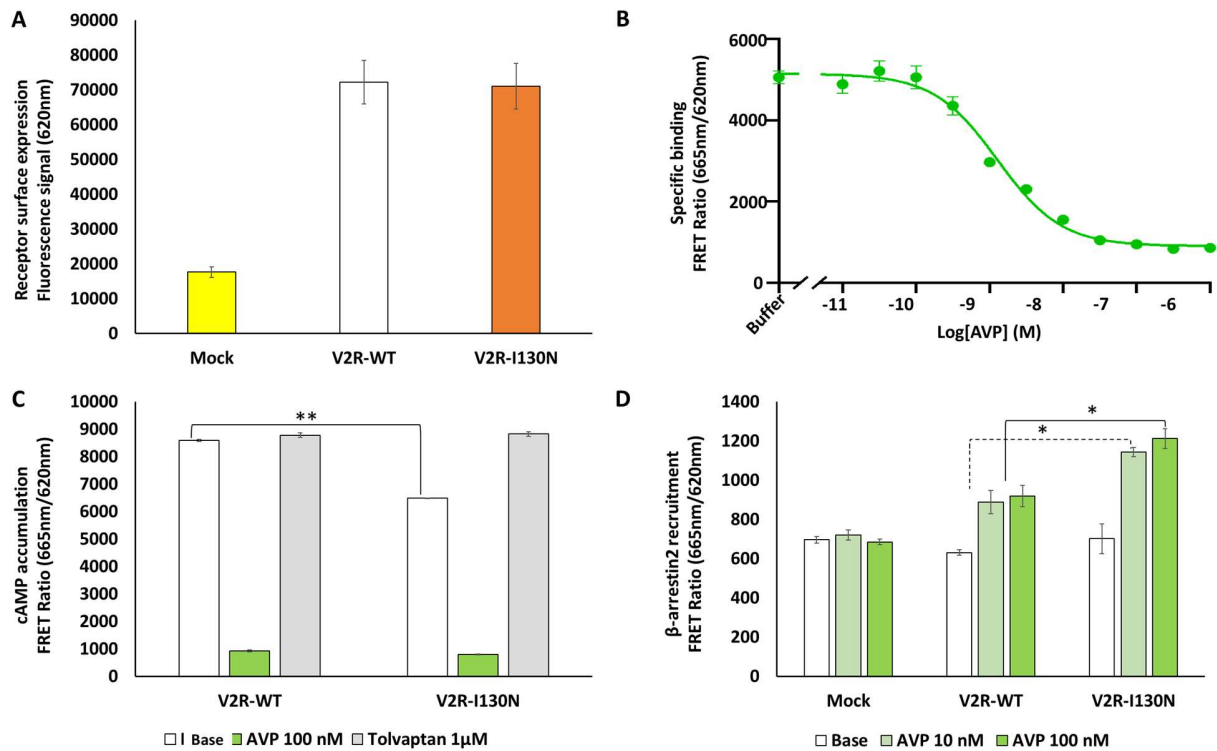


Figure S11. Pharmacological and functional properties of the mutant V2R^{I130N}. (A) Evaluation of the receptor expression level at the cell surface by measuring the fluorescence signal at 620 nm. The expression of the I130N mutant is compared to that of the WT V2R (see Material and Methods section for details, in these experiments, 30 ng for both plasmids were used). (B) Binding of AVP to the mutant V2R^{I130N} is illustrated as the FRET ratio (665 nm/620 nm x 10,000). Specific binding of the fluorescent benzazepine-red antagonist is shown. For each competition curve, the tracer was used at 5 nM with or without increasing concentrations of AVP. (C) Basal and ligand-induced V2R-dependent cAMP accumulation measured by the FRET ratio (665 nm/620 nm x 10,000). The functional properties of the mutant V2R^{I130N} are compared to those of V2R-WT. The cAMP accumulation is compared to that measured in the presence of 100 nM of AVP (in green) or 1 µM of TVP (in grey). (D) V2R-dependent recruitment of βArr2 to AP2 measured by the FRET ratio (665 nm/620 nm x 10,000) in the presence of 0 nM (base), 10 nM or 100 nM of AVP. The capacity of βArr2 recruitment of the mutant V2R^{I130N} is compared to that of V2R-WT. Data are mean ± SEM of 3 technical replicates where statistical significance is assessed by T-test (*, p < 0.05; **, p < 0.01).

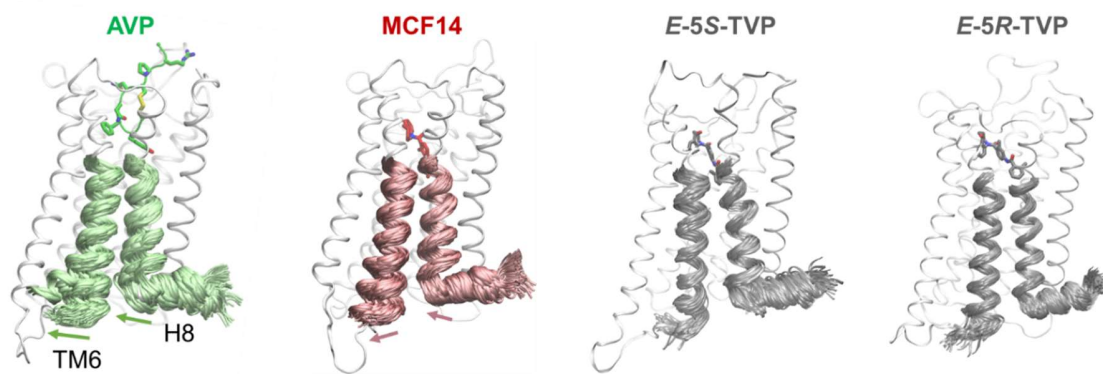


Figure S12. Conformational dynamics of V2R during MD simulations (related to Figure 3). Movements of TM6, TM7 and H8 on the intracellular side of V2R in the simulations. AVP-bound V2R was the most dynamic, whereas *E-5S-TVP* led to a closure of TM6 toward TM2. *E-5R-TVP* had minimal impact, leaving the receptor largely similar to the initial model.

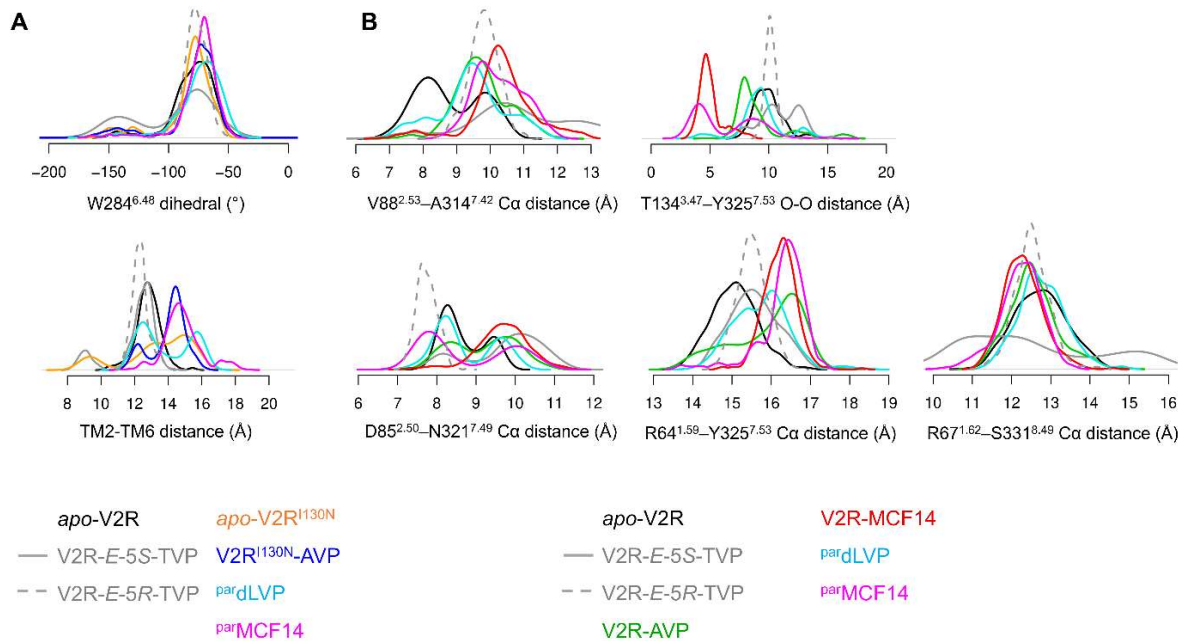


Figure S13. Probability density distribution of the conformational features measured during the MD simulations. (A) and (B) are supplementary to Figure 3, and Figures 5 and 6, respectively.

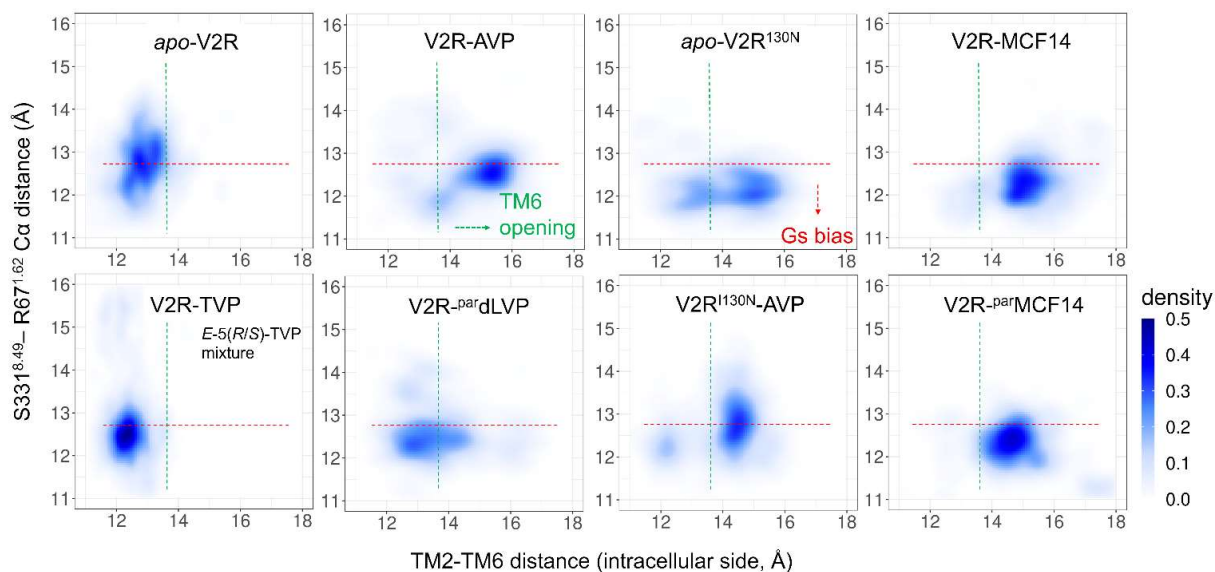


Figure S14. Probability density map of two conformational features during the MD simulations (related to Figures 3A, 5 and 6). TM6 opening (x-axis) is considered as an indicator of the canonical activation, whereas H8-TM1 closure (y-axis) is used as an indicator of the G-protein bias. TM6 opening is measured by the center-of-mass distance between the backbones of I74^{2.39}-F77^{2.42} and V266^{6.30}-T269^{6.33}. H8-TM1 closure is measured by the C α distance between S331^{8.49} and R67^{1.62}.

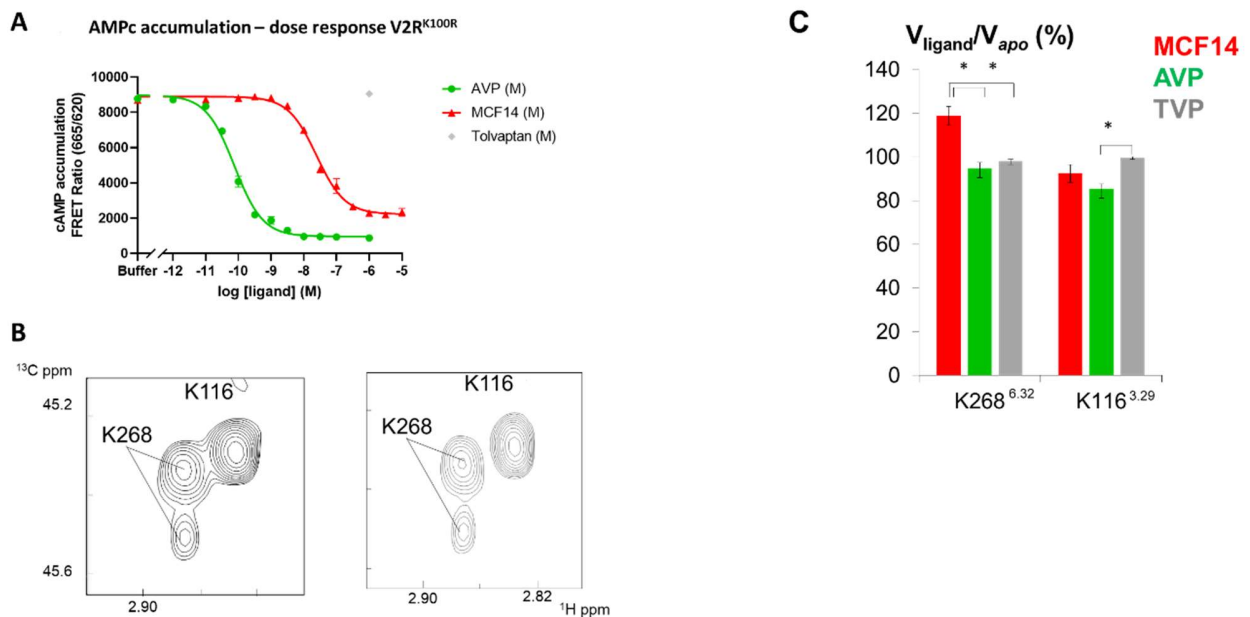


Figure S15. Functional and structural properties of V2R^{K100R} (related to Figure 3B).

(A) Ligand dose-response curves of V2R-dependent cAMP accumulation measured by FRET ratio (665 nm/620 nm x 10,000). The cAMP accumulation was quantified using the cAMP Gs Dynamic kit (PerkinElmer Revvity) as indicated in Material and Methods section and is shown in the presence of increasing concentrations of AVP (green), MCF14 (red), and TVP (in grey). Data are mean \pm SEM of 3 technical replicates. (B) Extracted HMQC spectra of V2R^{K100R} in *apo* form (black) and in the presence of saturating concentrations of the TVP antagonist (grey). The spectra of the *apo* and TPV-bound states are almost identical, indicating that the *apo* form is mainly inactive. (C) Analysis of peak volume changes of the NMR major peaks of V2R^{K100R} upon ligand binding. The K268 peak experiences an increase in volume in the MCF14 state compared to AVP, suggesting a different dynamic behavior of the TM6 cytoplasmic extremity. Values are mean \pm SEM of three (TVP and AVP) or four (MCF14) technical replicates, where statistical significance is assessed by T-test (*, $p < 0.05$).

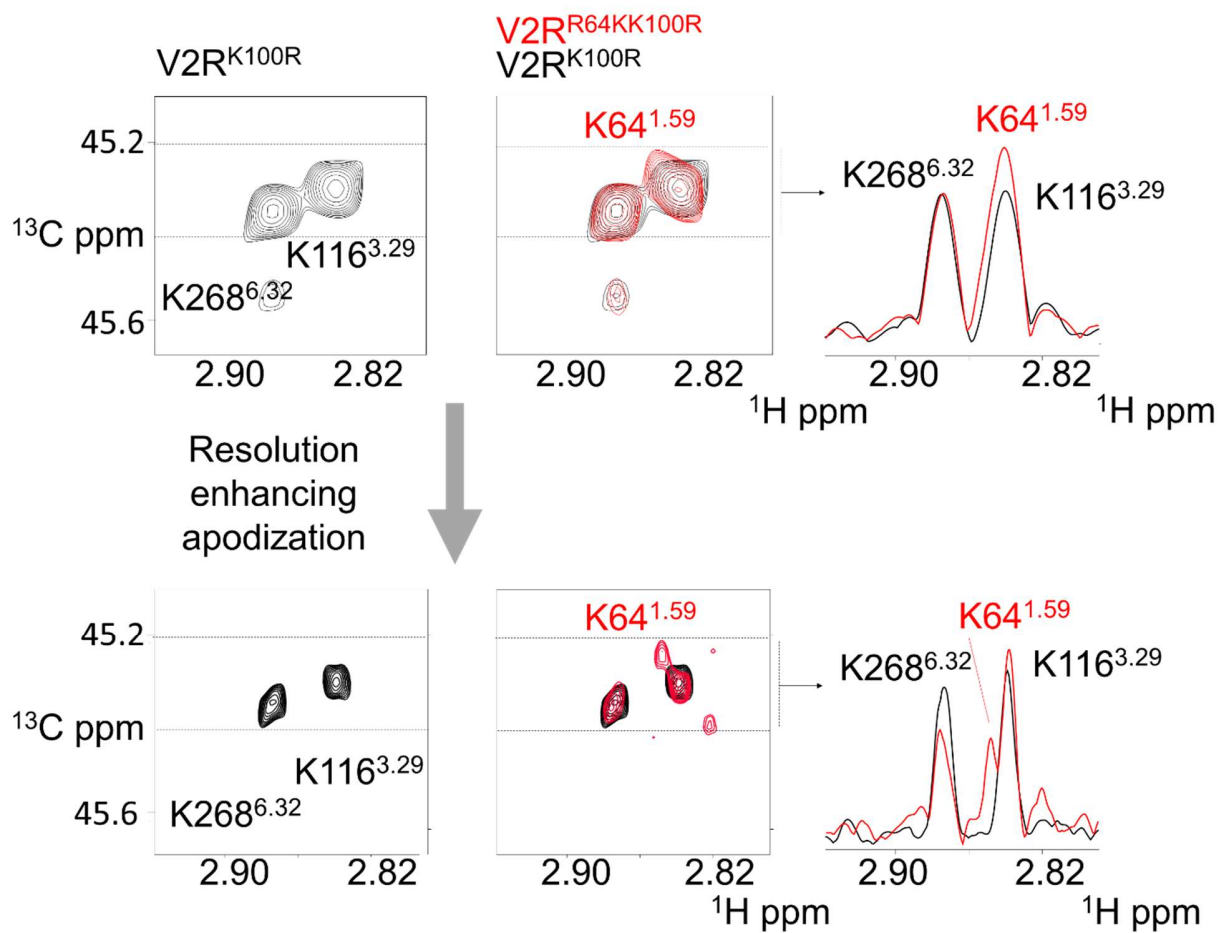


Figure S16. Assignment of correlation peak of the probe K64 of V2^{R64K-K100R}. Extracted HMQC spectra of V2^{K100R} (black) and V2^{R64K-K100R} (red). The bottom spectra are processed with a more resolution-enhancing sinus function. 1D spectra on the right correspond to 1D projections along the ¹³C dimension of ¹H rows between the two dashed lines.

Table S1. V2R systems studied.

Abbreviation	Ligand/ mutation	Gs activation	β Arr2 recruitment	References
<i>apo</i> -V2R	not applicable	-	-	
V2R-AVP	AVP	+	+	[1,2] and this study
V2R- ^{par} dLVP	^{par} dLVP	+	+	[3] and this study
V2R-MCF14	MCF14	+ (partial)	-	[4]
V2R- ^{par} MCF14	^{par} MCF14	+ (partial)	-	This study
V2R-TVP	Tolvaptan	-	-	[5] and this study
<i>apo</i> -V2R ^{I130N}	I130 ^{3.43} N	+ (constitutive)	-	[6]
V2R ^{I130N} -AVP	AVP	+	+	[6] and this study

Table S2. Ligand binding affinity for WT V2R and variants.

Receptor	K_d Benzazepine- red (nM)	K_i AVP (nM)
V2R-WT	2.3 ± 0.3 ¹	0.9 ± 0.3 (n=5)
V2R ^{K100R}	2.3 ± 1	3.2 ± 2.1
V2R ^{K116R}	8.5 ± 1.9	3.4 ± 0.8
V2R ^{K268R}	2.9 ± 1.3	2.0 ± 1.3
V2R ^{I130N}	6.6 ± 2.5	1.4 ± 0.6

¹ from ref [7]. Competitive binding experiments were performed as detailed in the Material and Methods section, using the benzazepine-red fluorescent ligand as a tracer. Specific binding of the benzazepine-red antagonist is calculated as a FRET ratio (665 nm/620 nm). K_d and K_i values are mean \pm SEM (n = 3, unless otherwise indicated).

Table S3. Ligand binding affinity and potency for V2R^{K100R} variant.

	Binding (K _i nM)	cAMP accumulation (EC ₅₀ nM)
AVP	3.2 ± 2.1	0.12 ± 0.05
MCF14	11.4 ± 0.4	26.9 ± 3.3
Tolvaptan	1.3 ± 0.4	n.a ¹

¹ n.a: not applicable

Competitive binding experiments were performed as detailed in the Material and Methods section, using the benzazepine-red fluorescent ligand as a tracer. Specific binding of the benzazepine-red antagonist is calculated as a FRET ratio (665 nm/620 nm). Accumulation of cAMP is calculated as a FRET ratio (665 nm/620 nm) and measured in the presence of increasing concentrations of ligands (AVP, MCF14, TVP). K_i and EC₅₀ values are mean ± SEM (n = 3).

SI References

- [1] R.H. Oakley, S.A. Laporte, J.A. Holt, L.S. Barak, M.G. Caron, Association of beta-arrestin with G protein-coupled receptors during clathrin-mediated endocytosis dictates the profile of receptor resensitization, *J. Biol. Chem.* 274 (1999) 32248–32257. doi:10.1074/jbc.274.45.32248.
- [2] J. Orloff, J.S. Handler, The similarity of effects of vasopressin, adenosine-3',5'-phosphate (cyclic AMP) and theophylline on the toad bladder, *J. Clin. Invest.* 41 (1962) 702–709. doi:10.1172/jci104528.
- [3] R.D.J. Kimbrough, W.D. Cash, L.A. Branda, W. Chan, V. Du Vigneau, Synthesis and Biological Properties of 1-Desamino-8-lysine-vasopressin, *J. Biol. Chem.* 238 (1963) 1411–4. doi:10.1016/S0021-9258(18)81197-8.
- [4] F. Jean-Alphonse, S. Perkowska, M.-C.C. Frantz, T. Durroux, C. Mejean, D. Morin, S. Loison, D. Bonnet, M. Hibert, B. Mouillac, C. Mendre, Biased agonist pharmacochaperones of the AVP V2 receptor may treat congenital nephrogenic diabetes insipidus, *J Am Soc Nephrol.* 20 (2009) 2190–2203. doi:10.1681/asn.2008121289.
- [5] Y. Yamamura, S. Nakamura, S. Itoh, T. Hirano, T. Onogawa, T. Yamashita, Y. Yamada, K. Tsujimae, M. Aoyama, K. Kotosai, H. Ogawa, H. Yamashita, K. Kondo, M. Tominaga, G. Tsujimoto, T. Mori, OPC-41061, a highly potent human vasopressin V2-receptor antagonist: pharmacological profile and aquaretic effect by single and multiple oral dosing in rats, *J Pharmacol Exp Ther.* 287 (1998) 860–867.
- [6] L.S. Erdélyi, W.A. Mann, D.J. Morris-Rosendahl, U. Groß, M. Nagel, P. Várnai, A. Balla, L. Hunyady, Mutation in the V2 vasopressin receptor gene, AVPR2, causes nephrogenic syndrome of inappropriate diuresis, *Kidney Int.* 88 (2015) 1070–78. doi:10.1038/ki.2015.181.
- [7] J. Bous, H. Orcel, N. Floquet, C. Leyrat, J. Lai-Kee-Him, G. Gaibelet, A. Ancelin, J. Saint-Paul, S. Trapani, M. Louet, R. Sounier, H. Déméné, S. Granier, P. Bron, B. Mouillac, Cryo-electron microscopy structure of the antidiuretic hormone arginine-vasopressin V2 receptor signaling complex, *Sci. Adv.* 7 (2021) eabg5628. doi:10.1126/sciadv.abg5628.